SOLAR WIND ELECTRON PROTON ALPHA MONITOR (SWEPAM) FOR THE ADVANCED COMPOSITION EXPLORER

D. J. McCOMAS, S. J. BAME, P. BARKER, W. C. FELDMAN, J. L. PHILLIPS and P. RILEY
Los Alamos National Laboratory, Los Alamos, NM 87545, U.S.A.

J. W. GRIFFEE
Sandia National Laboratory, Albuquerque, NM 87185, U.S.A.

Abstract. The Solar Wind Electron Proton Alpha Monitor (SWEPAM) experiment provides the bulk solar wind observations for the Advanced Composition Explorer (ACE). These observations provide the context for elemental and isotopic composition measurements made on ACE as well as allowing the direct examination of numerous solar wind phenomena such as coronal mass ejections, interplanetary shocks, and solar wind fine structure, with advanced, 3-D plasma instrumentation. They also provide an ideal data set for both heliospheric and magnetospheric multi-spacecraft studies where they can be used in conjunction with other, simultaneous observations from spacecraft such as *Ulysses*. The SWEPAM observations are made simultaneously with independent electron and ion instruments. In order to save costs for the ACE project, we recycled the flight spares from the joint NASA/ESA *Ulysses* mission. Both instruments have undergone selective refurbishment as well as modernization and modifications required to meet the ACE mission and spacecraft accommodation requirements. Both incorporate electrostatic analyzers whose fan-shaped fields of view sweep out all pertinent look directions as the spacecraft spins. Enhancements in the SWEPAM instruments from their original forms as *Ulysses* spare instruments include (1) a factor of 16 increase in the accumulation interval (and hence sensitivity) for high energy, halo electrons; (2) halving of the effective ion-detecting CEM spacing from $\sim 5^\circ$ on *Ulysses* to $\sim 2.5^\circ$ for ACE; and (3) the inclusion of a 20° conical swath of enhanced sensitivity coverage in order to measure suprathermal ions outside of the solar wind beam. New control electronics and programming provide for 64-s resolution of the full electron and ion distribution functions and cull out a subset of these observations for continuous real-time telemetry for space weather purposes.

1. Introduction

The Advanced Composition Explorer (ACE) mission was developed to examine both the isotopic and elemental composition of our Galaxy from the four reservoirs of matter that are accessible to a direct measurement from near the Earth. The first two of these reservoirs connect back to the Sun through the solar wind and through solar energetic particles, the third traces to the local interstellar medium (which is also the source population for anomalous cosmic rays) by way of locally ionized interstellar neutrals which form singly charged ions that are then picked up by the solar wind, and the fourth traces to our Galaxy at large by way of galactic cosmic rays. These observations are carried out with a suite of six experiments,

Space Science Reviews **86:** 563–612, 1998.

which jointly measure ion composition over the energy range from ~100 eV to several hundred MeV per nucleon, with sensitivities that are one to two decades larger than previously achieved. In addition, ACE carries three experiments that monitor the interplanetary medium, thereby providing the context for the advanced ion-composition experiments aboard ACE. These experiments are the Solar Wind Electron Proton Alpha Monitor (SWEPAM), the energetic Electron, Proton and Alpha particle Monitor (EPAM), and two magnetometers (MAG).

SWEPAM plays a critical role in ACE by providing the solar wind observations that enable the understanding of the ACE composition measurements in the context of previous knowledge about the solar wind. This knowledge has been developed over more than three decades of solar wind research. Specifically, SWEPAM will place the ACE composition measurements in the context of low-speed streamer belt flows, the high-speed solar wind from coronal holes, coronal mass ejections (CMEs), the various types and strengths of interplanetary shocks, magnetic connection to the Earth's bow shock, and other solar wind structures. Table I, from the ACE project's Level 1 requirements definition, lists the scientific objectives of the ACE mission. SWEPAM is considered a primary measurement (P) for six of these objectives and an important contributing measurement (C) for another five. Thus, SWEPAM measurements of the solar wind provide one of the critical cornerstones for the ACE mission.

The SWEPAM experiment provides state-of-the-art measurements of electron and ion distribution functions in three dimensions over all of the velocity space needed to characterize the bulk flow and kinetic properties of the solar wind. SWEPAM utilizes the refurbished flight spare instruments from the Solar Wind Over the Poles of the Sun (SWOOPS) experiment (Bame et al., 1992) onboard the joint NASA/ESA *Ulysses* mission. *Ulysses* was launched on October 6, 1990. It was deflected out of the ecliptic plane into its present high-inclination polar orbit about the Sun, using a gravitational assist at Jupiter, in late February 1992. SWOOPS has operated flawlessly since launch, thereby allowing exploration of the solar wind as a function of heliolatitude for the first time. Figure 1 summarizes the SWOOPS solar wind speed observations as a function of latitude in a polar plot format, similar to that shown by McComas et al. (1998). Note that while the high latitude solar wind is a comparatively steady flow of high-speed wind from both polar coronal holes, the low-latitude wind where ACE will reside is a complicated mixture of slow flows from the streamer belt and higher speed coronal hole flows.

The SWOOPS experiment comprises two separate instrument units, one for electrons and one for ions. These instruments, although different in size and detail, are based on the same basic principles. Both are electrostatic energy per charge (E/q) analyzers followed by sets of channel electron multiplier (CEM) sensors, which allow individual particles transmitted through the analyzers to be counted. In both cases, full complements of low and high voltage power supplies, memory, data processing capabilities, and spacecraft interfaces are provided as a part of the package such that each of the two instrument units is operated completely

TABLE I
ACE level 1 science objectives

	CRIS	SIS	ULEIS	SEPICA	SWIMS	SWICS	EPAM	SWEPAM	MAG
Composition of matter									
Generate table of solar isotropic abundance		P	P	P	P	C	C	C	
Determine coronal composition		P	P	P	P	P	C	P	
Compare cosmic-ray and solar isotope pattern	P	P	P	P	P	C	C	C	
Measure interstellar/interplanetary pickup ions				C	C	P		C	C
Determine anomalous cosmic-ray composition	P	P	P	C			C		
Origin/evolution of elements									
Identify solar/meteoritic composition differences		P	P	P	P	P	C	C	
Solar particle contributions to Moon/planets/meteorites		P	P	C	P	P	C	C	
Identify cosmic-ray nucleosynthesis process	P	P							
Determine age of cosmic-ray source material	P	P							
Search for evidence of galactic evolution	P	P	P	C	P	C			
Corona formation/solar wind acceleration									
Isolate coronal formation processes		P	P	P	P	P	C	P	
Study solar plasma conditions				P	P	P		P	C
Study solar wind acceleration/fractionation					P	P		P	P
Particle acceleration/transport									
Fractionation in solar flare/interplanetary acceleration		P	P	P	P	P	C	P	C
Constrain particle acceleration models	P	P	P	P	P	P	P	P	P
Test 3 He-rich and gamma-ray flare models	C	P	P	P			P	P	C
Measure cosmic-ray acceleration/transport time scale	P	P							
Test anomalous cosmic-ray origin	P	P	P	P					

P = primary measurements.
C = contributing measurements.

TABLE I
Continued

Acronym	Name	Lead institution
CRIS	Cosmic-Ray Isotope Spectrometer	CIT
EPAM	Electron, Proton, and Alpha-Particle Monitor	APL
MAG	Magnetic Field Monitor	Bartol
SEPICA	Solar Energetic Particle Ionic Charge State Analyzer	UNH
SIS	Solar Isotope Spectrometer	CIT
SWEPAM	Solar Wind Electron, Proton, and Alpha-Particle Monitor	Los Alamos
SWICS	Solar Wind Ion Composition Spectrometer	UMD
SWIMS	Solar Wind Ion Mass Spectrometer	UMD
ULEIS	Ultra Low Energy Ion Spectrometer	UMD

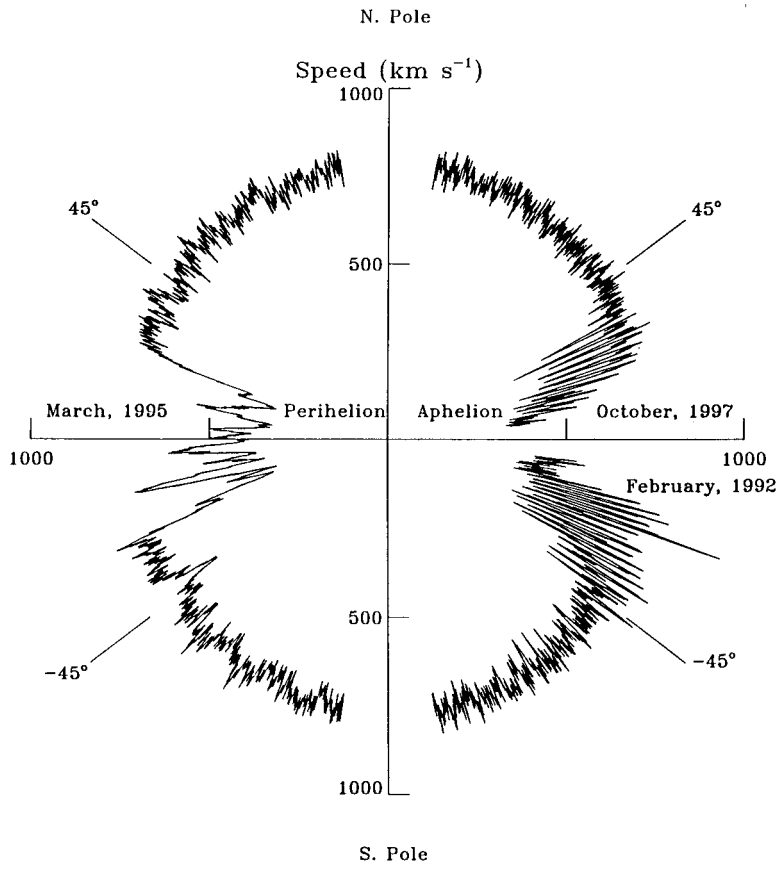

Figure 1. Polar plot of solar wind speed measured by the SWOOPS experiment on *Ulysses* over nearly one complete polar orbit about the Sun. Cyclic variations between high and low speeds, observed on the right side of the plot at mid-latitudes, are due to rotation of the Sun.

independently of the other. For the SWEPAM experiment on the ACE mission we have selectively modified, refurbished, and improved the SWOOPS flight spare instruments. In particular, SWEPAM provides enhanced sensitivity to suprathermal electrons ($E > 100$ eV) to allow a greater sensitivity for detecting CMEs and for establishing their magnetic topology and evolution in interplanetary space. SWEPAM also provides higher angular resolution measurements of solar wind ions as well as increased sensitivity to suprathermal ions coming from directions adjacent to the bulk solar wind in order to provide a bridge between the energetic ions detected using the suite of ACE composition experiments, and the solar wind thermal population.

This paper provides the primary documentation source for the ACE/SWEPAM experiment. In Section 2 we briefly review solar wind science and place the anticipated SWEPAM observations and scientific results in the context of previous observations. Sections 3 and 4 provide detailed descriptions of the SWEPAM ion and electron instruments, respectively. In each we: (1) summarize the electro-optical properties and general specifications of the sensor, (2) show the mechanical design of the sensor, (3) discuss the electronics associated with each instrument, and (4) show the results of sensor calibrations. While sufficient detail is given for the interested reader to understand the implemented mechanical and electronics designs, these two sections are arranged so that the detailed subsections can be skipped without losing an understanding of the top-level design. Section 5 describes the commanding, data handling, modes of operation, and the real-time solar wind capability of SWEPAM.

2. Scientific Objectives

The primary purpose served by SWEPAM is to provide the solar wind context for the other experiments on ACE. Connection to global heliospheric structure will be facilitated by correlation of SWEPAM data with simultaneous measurements made using the SWOOPS experiment on *Ulysses*. During the early portion of the ACE mission, *Ulysses* will be positioned near 5.4 AU, close to the ecliptic plane. The heliographic locations of ACE relative to *Ulysses* between 1997 and 2002 are shown in Figure 2. Times of longitudinal lineup are indicated by the intersections between the dotted and solid traces in the top panel. These lineups occur in early 1998, 1999, and 2000.

It will also be critical to place the new ACE observations in the context of synoptic changes in solar wind structure that are associated with phases of the solar cycle. The time period of the ACE mission will extend from near solar minimum toward the coming solar maximum. Over this portion of a solar cycle the photospheric and coronal magnetic fields evolve from simple, dipolar-like configurations, with axes nearly perpendicular to the ecliptic plane, to configurations of considerable complexity. This complexity is characterized by a rapid spatial evolution of the

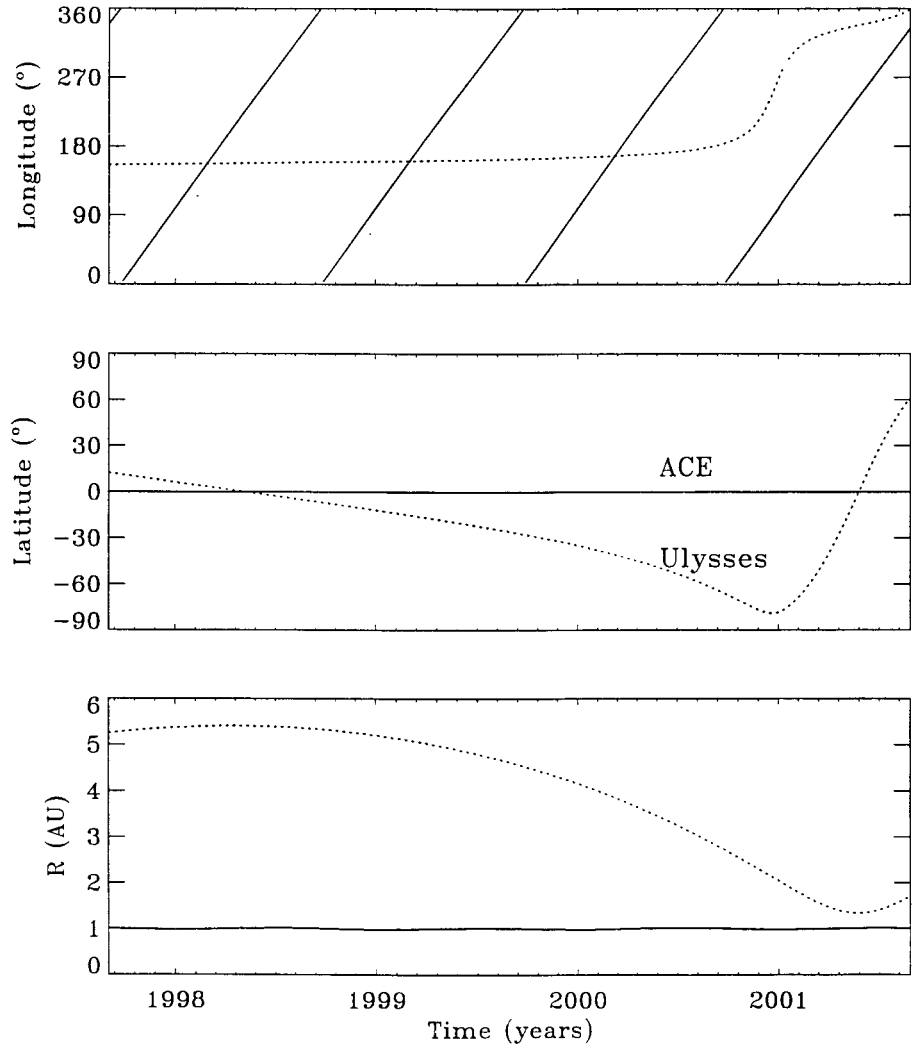

Figure 2. Heliographic longitudes, latitudes, and radial distances of ACE and *Ulysses*, spanning the period from the launch of ACE in late 1997 through 2002.

photospheric magnetic field and accompanying time variability, first associated with the appearance of magnetic active regions at relatively high heliographic latitudes, and later to their appearance at progressively more equatorial latitudes. Understanding ACE observations as a function of the solar activity cycle will be facilitated by comparison of these observations with measurements made from the particle and fields experiments onboard ISEE-3 in the late 1970s and early 1980s. These observations were made from the same Sun–Earth–L1 neighborhood to be occupied by ACE, but in a previous solar cycle. Specific contributions by

SWEPAM in support of a number of the major scientific thrusts of the ACE mission are presented below.

2.1. FORMATION OF THE SOLAR CORONA AND ACCELERATION OF THE SOLAR WIND

Synoptic studies of solar and solar wind structure during the 1970s revealed an evolving global configuration that followed the pattern of changes in photospheric and coronal magnetism mentioned above. Near solar minimum, the global solar wind consists of high-speed flows emanating from both solar poles separated by a roughly planar, low-speed streamer belt at equatorial latitudes that is nearly parallel to the ecliptic plane (see Figure 20(d) of Hundhausen, 1977). A similar global structure was observed by *Ulysses* during its fast-latitude scan from $-80.2°$ to $+80.2°$ heliographic latitude between September 1994 and August 1995, as shown on the left side of Figure 1. This interval occurred just prior to the minimum of solar activity during the present activity cycle. An expanded version of this traversal, including the observed proton density scaled to 1 AU, is shown in Figure 3 (assembled by B. E. Goldstein using SWOOPS plasma data and a *Yohkoh* X-ray image of the corona, kindly provided by the *Yohkoh* mission of ISAS, Japan). *Ulysses* observed nearly structure-free, high-speed solar wind ($V > 700$ km s^{-1}) for all heliographic latitudes poleward of about 22°, and variable, but generally low-speed solar wind equatorward of 22°. This high-speed–variable-speed transition was recently reconfirmed by *Ulysses* as it approached aphelion within about 29° of the ecliptic plane (upper right quadrant of Figure 1) (McComas et al., 1998).

If these conditions prevail throughout the early portion of the ACE mission, as expected, then phenomena associated with the streamer belt and its embedded heliospheric current sheet will dominate observations made by all experiments onboard ACE (see the yellow stripe in the bottom panel of Figure 3). Observations made by ISEE-3 during the same phase of the solar cycle between 1978 and 1980, and by *Ulysses* just after its launch early in the current solar cycle, suggest that ACE will also likely spend a fraction of its time in those portions of the coronal-hole-associated high-speed streams that are adjacent to streamer-belt flows. Transitions between streamer-belt and coronal-hole-associated flows correspond to the flow-speed variability encountered by *Ulysses* at intermediate heliographic latitudes shown in Figures 1 and 3. The correspondence between the solar wind flow state observed by *Ulysses* and the structure of the corona as observed in X-rays by *Yohkoh*, is shown by comparing the panels in Figure 3. The high-speed wind is clearly associated with the large polar coronal holes. While most, if not all, of the solar wind must expand along open field lines, the low-speed wind seems to be associated with the bright, largely closed magnetic structures. The intermediate and variable solar wind appears to come from the margins between these two regions.

During the approach to solar maximum, an ever increasing number of magnetically active regions rise through the photosphere. These then interact both with

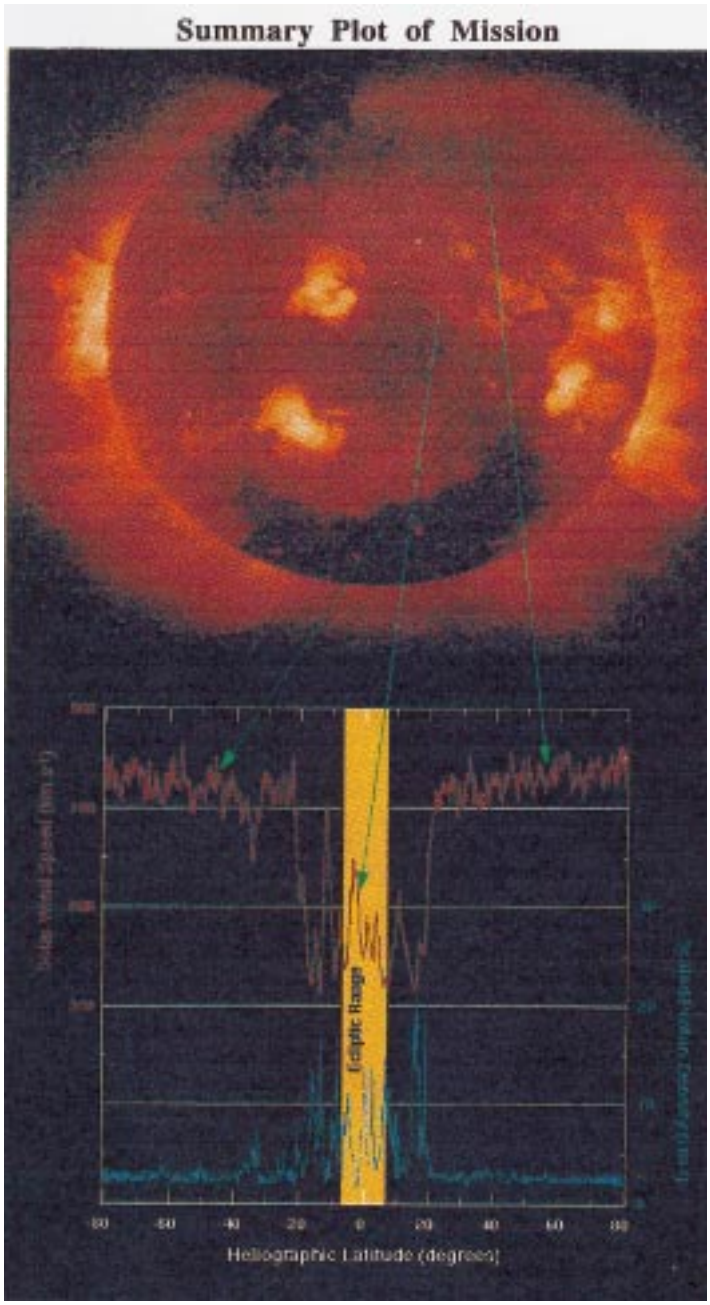

Figure 3. Identification of the solar wind flow state, as given by the proton bulk speed and density (projected to 1 AU), measured by *Ulysses* during its fast latitude scan, compared with the configuration of the solar corona, as measured in soft X-rays by *Yohkoh*. *Yohkoh* data was kindly provided by the *Yohkoh* mission of ISAS, Japan.

the preexisting dipolar magnetic field and with each other, producing a series of rapid reconfigurations that contribute to a pattern of solar magnetism characterized by a regular (and at times, extreme) time variability. These reconfigurations lead to an increasingly complex magnetic configuration. The global structure of the corona and resultant solar wind change accordingly in response to these underlying changes. In particular, an ever greater fraction of the solar wind encountered far from the Sun is associated with coronal mass ejections (CMEs) and other transient flows. In addition, some of the apparently time-stationary high-speed flows encountered outside of the streamer belt originate from relatively small unipolar photospheric regions that evolve on timescales of months, in contrast to the timescale of years over which the much larger area coronal holes evolve near solar minimum.

Although much is already known about the evolution of the large-scale pattern of solar wind structure in response to the solar activity cycle, very little is known about the mechanisms that connect the flow state of the slow wind with plasma conditions in the corona. Even more fundamental, we do not yet know the mechanisms that heat the solar corona and accelerate its plasma outward to form the solar wind. One of the major scientific goals of SWEPAM is to provide the link between the data from the composition experiments on ACE and the sources of the various types of solar wind back in the solar corona.

2.1.1. *Streamer Belt*

Bright, high-density streamers are clearly seen during solar eclipses and are prominent in coronagraph images of the Sun. These streamers, which are also associated with the equatorial bright regions seen in the soft X-ray images of the Sun (e.g., Figure 3), give rise to highly structured but slow solar wind flows. These flows are characterized by large variations in speed, density, temperature, heat flux, helium abundance, and heavy ion charge-states (e.g., Feldman et al., 1977, 1981; Borrini et al., 1981). Some of these variations probably reflect fine spatial-scale structure in the streamer belt owing, at least in part, to the meandering of the neutral line in the photosphere. The interplanetary extension of this neutral line is a current sheet that is embedded in streamer belt associated flows. In addition, variability in the low-speed wind may be caused by quasi-continuous, fine-scale magnetic restructuring at low altitudes above the photosphere (Axford, 1985). Some of this restructuring may be caused by the different rate of rotation of fine-scale photospheric magnetic fields relative to that of the deep-seated currents that are responsible for large-scale patterns of solar magnetism (Sheeley et al., 1975), and some may be due to the emergence and decay of active regions within the streamer belt.

Attempts have been made to associate peculiarities in the internal state of solar wind ions and electrons with each of the foregoing possibilities, without definitive success. The problem in interpretation stems from essential ambiguities in relating the plasma at 1 AU with production mechanisms in the corona. A partial list of solar wind observables includes: (1) double ion streams as shown in Figure 4,

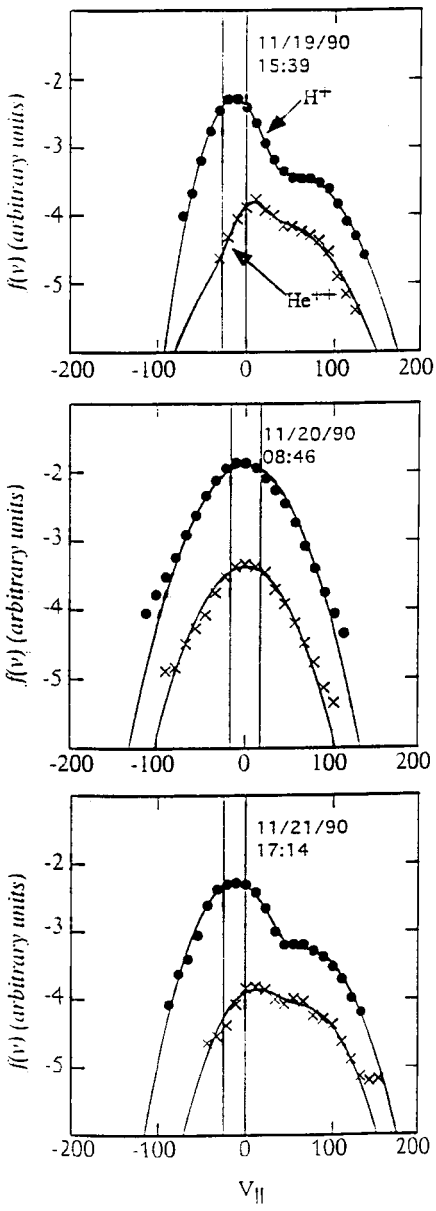

Figure 4. Evidence for magnetic reconnection within the streamer belt as shown by SWOOPS observations of double proton and alpha-particle streams on either side of (top and bottom panels), but not at the center of (center panel) the heliospheric current sheet.

possibly driven by magnetic reconnection (Hammond et al., 1995; Feldman et al., 1996); (2) heat flux dropouts, possibly signifying magnetic disconnection from the corona (McComas et al., 1989); (3) heat flux enhancements, possibly caused by transient-driven shocks that are magnetically connected to the spacecraft, (Feldman and Marsch, 1997); (4) non-compressive density enhancements (NCDEs) (Gosling et al., 1977); (5) the intensity and shape of suprathermal electron velocity distributions, possibly signifying major magnetic restructuring of the inner heliosphere; (Gosling et al., 1987; Feldman and Marsch, 1997); and (6) the He to H relative abundance variations, which may be caused by changes in the structure of the chromosphere-corona transition zone (e.g., von Steiger and Geiss, 1989). A major scientific objective of the SWEPAM experiment is to relate such observables to peculiarities in isotopic and elemental abundances measured by the composition experiments on ACE.

2.1.2. *Coronal Mass Ejections*

The interplanetary manifestations of CMEs in the solar wind are varied. Perhaps the single best identifier is the occurrence of counter-streaming suprathermal electrons (e.g., Gosling, 1996, and references therein). The appearance of CMEs in coronagraph images shows radially evolving sets of structured loops of enhanced density; these structures are interpreted as tracing sets of nested magnetic loops that are closed at both ends to the Sun. Connection to the hot corona at both ends of these loops should, in turn, drive an outward-directed electron heat flux along both coronal footpoints. The consequent field-aligned streams of suprathermal electrons that carry this heat flux are thought to be the counter-streaming electron signatures observed in interplanetary space. An example of such a signature is shown in C and D of Figure 5 (from McComas et al., 1994). By comparison, regions A and E show more typical halo electron distributions where direct connection to the hot corona is made in only one direction along the magnetic field.

Although the presence of counter-streaming suprathermal electrons is highly likely, it is neither a necessary nor a sufficient interplanetary signature of a CME. Many other plasma and magnetic field identifiers have also been associated with CMEs in the solar wind. These identifiers include: (1) a generally enhanced helium abundance that is often characterized by large temporal and/or spatial variations (Hirshberg et al., 1972); (2) unusually low ion and electron temperatures (Gosling et al., 1973; Montgomery et al., 1974); (3) macroscopic rotations of the IMF interpreted as a magnetic cloud (Klein and Burlaga, 1982); (4) charge states of heavy ions that indicate a coronal temperature larger than about 2×10^6 K (Bame et al., 1979); and (5) counter-streaming suprathermal ions (Marsden et al., 1987).

The solar wind identified with CMEs is often highly structured. Not only do the various observables used to identify a CME often vary considerably during any given event, they often do not coexist in any given parcel of CME plasma. Indeed, sometimes they do not even overlap spatially. These observations have led to a picture of CMEs in the solar wind as consisting of a raisin-pudding conglomerate

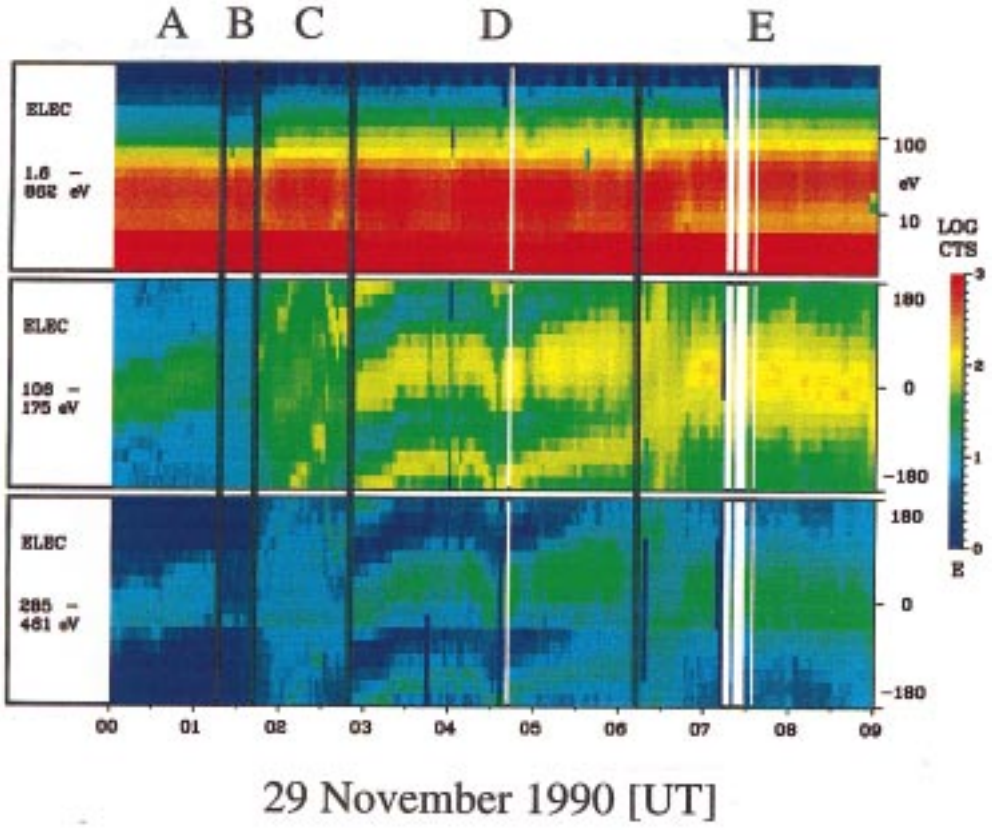

Figure 5. Color-coded plots of suprathermal electron counts for a CME (C, D) observed by *Ulysses* on 29 November 1990. Region B displays a heat flux dropout, which may signify a region that is magnetically disconnected from the corona at either end while regions A and E show typical mono-directional electron heat fluxes. Figure taken from McComas et al. (1994).

of small-scale structures convecting together in the ambient interplanetary medium. Figure 6 shows a schematic sketch of a CME in the solar wind that combines features presented by Bame et al. (1979) and Gosling and McComas (1987). This basic picture has been reinforced by recent observations of a CME observed simultaneously at high and low heliographic latitudes by *Ulysses* and IMP-8 (Gosling et al., 1995). It is curious that while the He abundance in this CME was >10% at times at low latitude, in the same CME at high latitude, it remained constant at the high-speed wind value of ~4.4% (Barraclough et al., 1996).

2.1.3. *Outstanding Questions*

A common thread that connects streamer belt flows with CMEs is that they both originate from regions that overlie complex magnetic topologies in the photosphere that, at times, undergo large reconfigurations. The streamer belt generally overlies most zones of high magnetic activity that consist of complex, strong magnetic

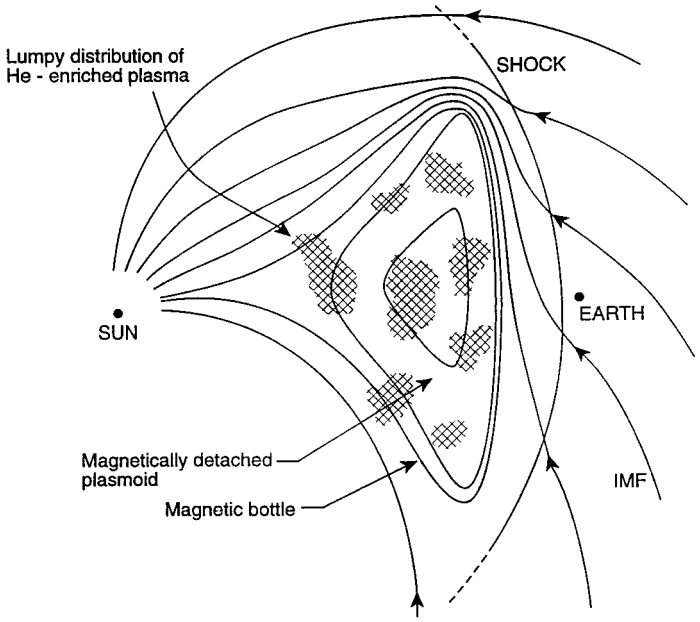

Figure 6. Schematic diagram of a CME that drives a shock wave in the ambient upstream solar wind. The hypothetical disturbance that is sketched contains both a plasmoid (magnetically disconnected from the Sun) and a bottle (magnetically connected to the Sun at two footpoints). The entire disturbance is filled with isolated patches of He-enhanced plasma that cross boundaries between the three different magnetic topologies present in interplanetary space.

field configurations having a high multipolarity and a relatively short lifetime (e.g., Hundhasuen, 1977). CMEs are thought to result from a large-scale restructuring of longer-lived magnetic field structures (Low, 1996). Time sequence observations of the corona in white light (see, e.g., Hundhausen, 1988), EUV (Dere, 1994), and in X-rays (Tsuneta, 1996) have graphically illustrated the consequences of these reconfigurations on the structure of the transition region and overlying corona. These range from the ponderous uplift of large volumes of coronal gas (a CME) to the injection of fine-scale, high-speed jets of relatively cold (Hα surges and EUV explosive events, 10^4 to 10^5 K) and very hot (X-ray jets, 10^6 to 10^7 K) gas into the pre-existing, ambient solar wind.

All the foregoing phenomena and their consequent solar wind extensions to interplanetary space are intrinsically time dependent. Although the relatively gross aspects of their origin (free energy contained in the photospheric magnetic field), and their effects on the low corona (convected enthalpy and kinetic energy of plasma bulk motion), are known from remote-sensing observations, not very much is known about the mechanisms that drive them. It seems reasonable to presume that magnetic reconnection in some form is the prime mechanism that effects the transfer of energy from the preexisting magnetic field to the plasma and energetic particle population. However, we do not know the altitude at which reconnection

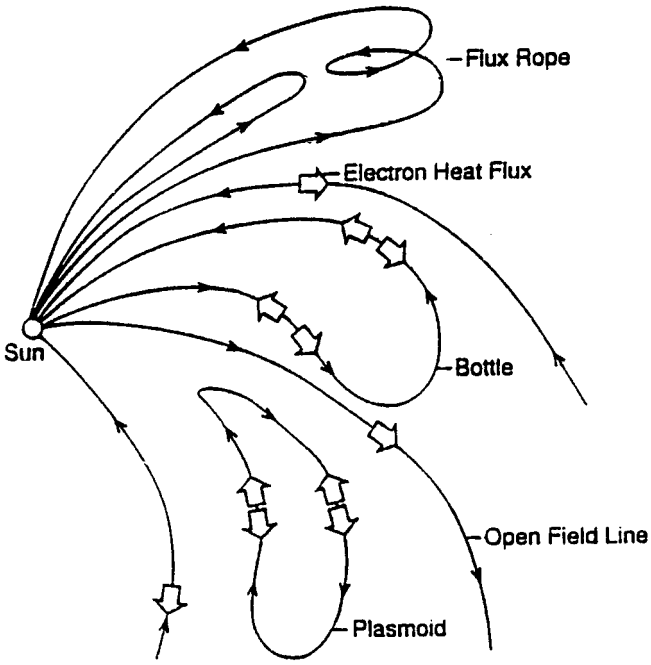

Figure 7. Schematic illustrations of four generic types of interplanetary magnetic topologies. At bottom is a simple open topology, connected at one end to the Sun and at the other end to the interstellar medium. Heat flux is expected to be unidirectional away from the Sun as shown by the arrow. Just above is a completely disconnected plasmoid. Heat flux is expected to be either absent or bidirectional. Next above is a magnetic bottle or tongue, connected at both ends to the Sun. The heat flux here is also expected to be bidirectional. At the top is pictured the simplest flux-rope topology. It is also connected at both ends to the Sun but contains one or more loops. Figure from Feldman and Marsch (1997).

is initiated. Nor do we know the plasma properties in regions that undergo reconnection, or the relative fraction of the magnetic energy that goes into plasma bulk motion, ion heating, electron heating, and the energetic particle population. Are magnetically-closed structures ever produced by this reconnection, or do they always produce complex flux-rope topologies containing a mixture of open, closed, and disconnected field lines (i.e., Gosling et al., 1995)? Schematic examples of several possible magnetic topologies are shown in Figure 7. What is the time scale of the initial reconnection event? Are slow-mode shocks generated by these events as suggested by Petschek (1964), and if so, what is the contribution to the plasma structure of the streamer belt? At what altitude are fast-mode shocks initiated? Do the flux ropes continue to evolve as they expand outward into the solar wind? Is there a component of the streamer belt flow at 1 AU that is not associated with solar activity (i.e., that is driven by a quasi-static pressure gradient as first suggested by Parker (1958))? If so, what is the heating mechanism that supports a quasi-static, million-degree corona and where does this heating occur?

Answers to many of these questions have been offered based on analyses of previous particle and fields observations. None of these, however, is definitive because of essential ambiguities in interpretations of most of the data that was available. Specifically, many characteristics of these data (such as plasma ion and electron temperature and particle energy spectra) are affected by so many processes that occur between the Sun and Earth that they contain highly ambiguous information about conditions near the coronal base where the solar wind is launched. However, the ambiguity in interpretation of the isotopic, elemental, and charge-state composition of plasma and energetic particles from the Sun is considerably reduced because these parameters do not change greatly above the coronal base during their transport to 1 AU. We therefore expect that it should be possible to make considerable progress in finding solid answers to many of the foregoing questions through a joint analysis of the solar wind data returned by SWEPAM and the composition measurements made by the comprehensive composition payload on ACE.

2.2. Particle acceleration and transport

Another major thrust of the ACE mission is to increase our understanding of the origin and evolution of the energetic particle populations that are found almost ubiquitously throughout the inner heliosphere. An important component of this population is accelerated in interplanetary space, and most of it must be transported across large distances in the solar wind before being detected at 1 AU. Numerous analyses have shown that the forward and reverse shocks that bound co-rotating interaction regions (CIRs) beyond 1 AU are copious accelerators of particles. An example of one such interaction region observed by *Ulysses* at 5 AU is shown in Figure 8 (Gosling et al., 1993). Note the large enhancements in the electron suprathermal population extending to considerable distances upstream from both the forward shock (day 20 ∼05:00) and reverse shock (day 22 ∼02:00) that bound the CIR. Other important sites of particle acceleration occur near forward shocks that are driven through the ambient plasma by fast CMEs.

The seed population for particle acceleration can originate in the thermal and suprathermal components of the solar wind, or in the population of pickup ions that are injected into the solar wind from the neutral component of the interstellar medium, which interpenetrates the inner heliosphere. This latter injection results from (1) charge-exchange collisions with solar wind ions; (2) photoionization by solar EUV photons; and (3) impact ionization by solar wind electrons. Although charge-exchange collisions and photoionization generally dominate impact ionization in the injection of interstellar neutrals into the solar wind, shock-heated electrons upstream of some CMEs can sometimes make important (and for helium, dominant) contributions, as illustrated by the impact ionization rate curves (marked with circles and squares) in Figure 9 (Isenberg and Feldman, 1995; Feldman et al., 1996).

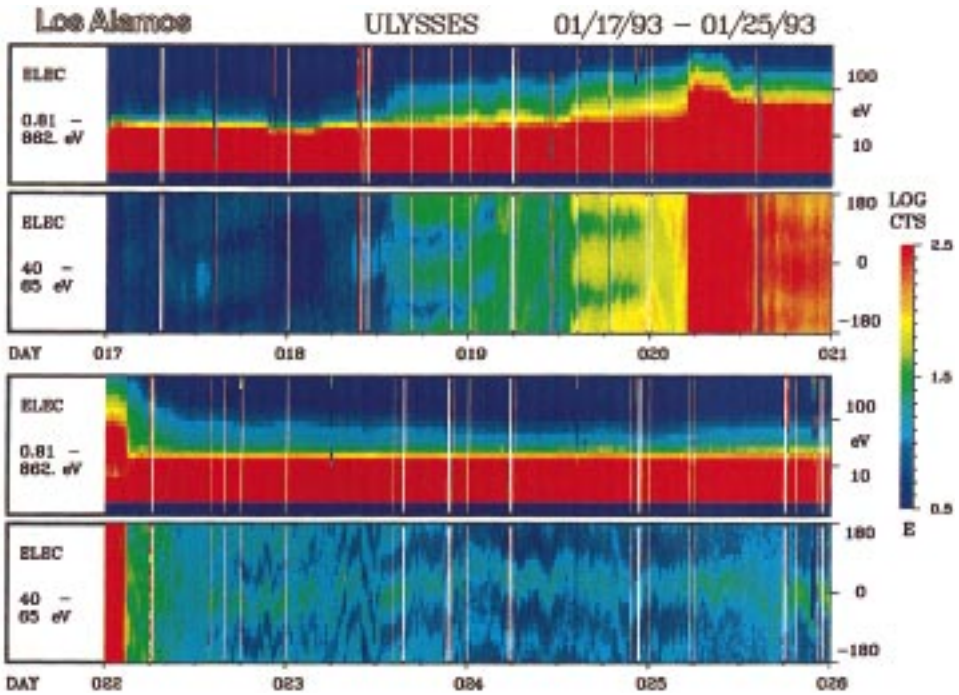

Figure 8. Color-coded plot of solar wind electron data for the co-rotating interaction region encountered by *Ulysses* at ∼5 AU in January 1993. Figure taken from Gosling et al. (1993).

Although the shapes of particle energy distributions largely result from processes that occur in the neighborhood of shocks, they evolve in important and characteristic ways while streaming from these shocks to their point of detection. This evolution is controlled both by the topology of the IMF that is carried by the solar wind and by the nature of the waves that fill interplanetary space. The effect of waves on energetic particles is enhanced if the magnetic topology is that of a complex flux rope or if the imbedded magnetic field intersects a shock front at more than one location. In such cases, the time available for scattering a seed particle in transit through a given interplanetary distance is longer and there is more time for interactions.

2.2.1. *Co-rotating Interaction Regions*

Shocks driven by co-rotating interaction regions do not generally form at radial distances less than about 2 to 3 AU, and so will only occasionally be directly detected by ACE near 1 AU. SWEPAM data can, however, be used to predict CIR onsets and their locations relative to Earth using appropriate MHD models. Predictions of these models can be checked using the solar wind observations made by the SWOOPS instrument onboard *Ulysses*, which will be located just beyond 5 AU near the ecliptic plane throughout the prime portion of the ACE mission (Figure 2). This combination of dual-point observations and MHD model predictions

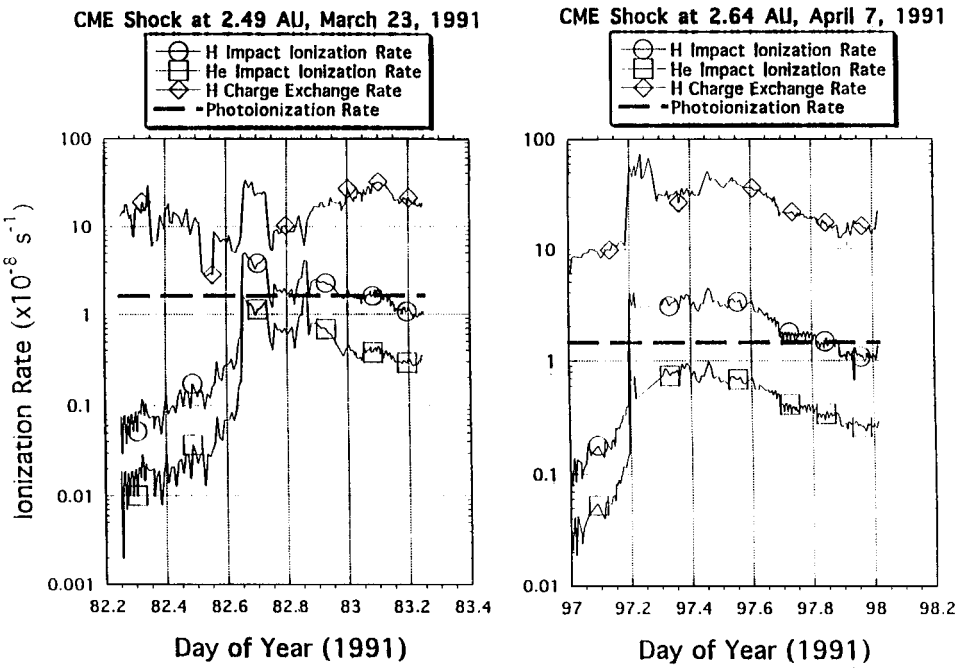

Figure 9. The various ionization rates of interstellar hydrogen and helium atoms calculated from data measured by *Ulysses* across two CME-driven shock wave disturbances. Identification of the ionization processes for the different curves is given in the legend. Figure taken from Feldman et al. (1995).

should provide the needed context for composition observations of backstreaming populations of energetic ions accelerated by the shock pairs that bound CIRs at large heliocentric distances.

2.2.2. *Forward Shocks*

Forward shocks, driven by fast CMEs, accelerate significant numbers of thermal and suprathermal ions and electrons to high energies (see, e.g., Figure 8). These shocks, and the associated enhanced populations of suprathermal ions and electrons, will be detected and fully characterized by SWEPAM. Special attention was given in upgrading the physical configuration of the SWEPAM ion analyzer, and in implementing data accumulation cycles for both plasma ion and electron experiments, to return fully three-dimensional energy-angle spectra having sufficient velocity-space resolution and counting statistics to provide a bridge between the solar wind thermal population and the energy spectra of energetic particles. The shapes of these distributions should be sufficiently detailed to enable definition of the magnetic topology of the ambient plasma through which the shocks propagate. This topology will be of fundamental importance in assessing the type and efficiency of acceleration processes at work at these shocks.

2.2.3. *Pickup Ions of Interstellar Origin*

SWEPAM data will also be used to support studies of the solar wind pickup of newly ionized interstellar neutral atoms. Most important for the pickup of interstellar hydrogen will be SWEPAM's measurement of the solar wind mass flux because the ionization rate is dominated by charge-exchange collisions with solar wind protons.

Past studies of ISEE-3 and *Ulysses* electron data show that just upstream and downstream of strong interplanetary shocks, electron impact ionization can enhance ionization and hence pickup of interstellar hydrogen atoms by roughly 10% (Isenberg and Feldman, 1995; Feldman et al., 1996). These same measurements also indicate that electron impact ionization can dominate photoionization for interstellar helium atoms (see, e.g., Figure 9). These effects are doubly significant because the subsequent acceleration of these newly injected ions to higher energy is enhanced in the neighborhood of shocks. SWEPAM data can also be used to help in studying particle transport through the solar wind by providing knowledge of the magnetic topology in the neighborhood of these shocks. This knowledge will result from study of the shapes and intensity of suprathermal electron and ion velocity distributions.

3. Solar Wind Ion Instrument (SWEPAM-I)

The solar wind ion instrument, SWEPAM-I, contains a spherical section electrostatic analyzer (ESA). Ions enter the sensor through its aperture and are immediately introduced into the gap between the electrostatic analyzer plates. A negative high voltage on the inner plate of the electrostatic analyzer biases the analyzer such that only ions within a narrow energy per charge range ($\sim$5%) and azimuthal angular range (3–4.5°, depending on polar angle) are permitted to pass through the analyzer. The transmitted ions are detected in the channel electron multipliers (CEMs) located immediately behind the analyzers. The aperture of the sensor is aligned such that its fan-shaped field-of-view rotates about the spacecraft spin axis. Figure 10 schematically displays the SWEPAM-I pointing and electro-optics. We define two angles through the normal to the sensor aperture: the polar angle, θ, in the plane of this fan (plane of the right hand sketch), where 0° is parallel to the Sun-pointing spin-axis direction of the ACE spacecraft. The azimuthal angle, ϕ, is in the plane perpendicular to the fan (plane of the left hand sketch).

The normal to SWEPAM-I's aperture is pointed 18.75° in polar angle away from the sunward pointing spin axis direction on the ACE spacecraft. This allows SWEPAM-I to measure ions arriving at polar angles from 0° (along the Sun-pointing spin axis) out to $\sim$65°. Ions in the main solar wind beam, which usually arrive from polar angles of $<$25°, are measured by CEMs on both sides of the fan. The offset angle of the sensor's pointing will interleave observations from one half of the rotation with those from the other half with a consequent improvement

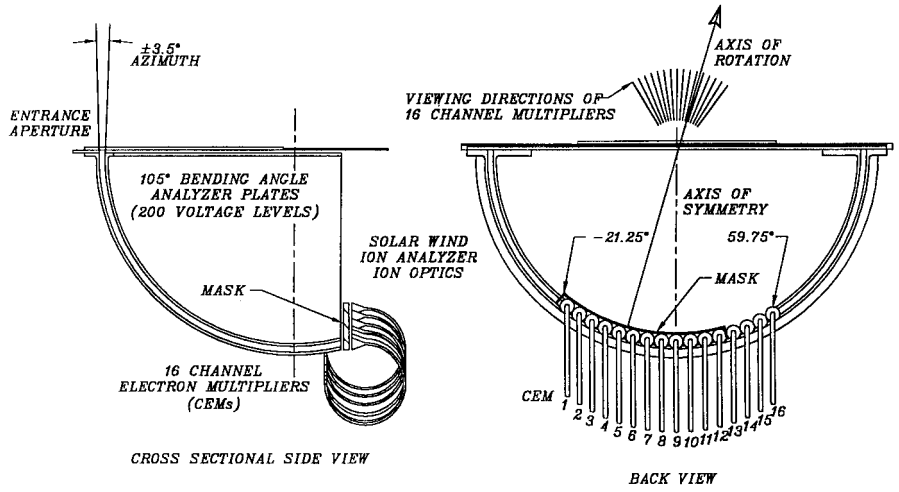

Figure 10. Schematic diagram of the SWEPAM-I electro-optics. The ion sensor is tilted with respect to the spin axis such that observations from CEMs 1-5 should interleave with those from CEMs 6-10. The exit aperture mask that has been added for SWEPAM is indicated in both images (see text).

in polar angle resolution from 5° down to 2.5°, if the spacecraft spin axis is perpendicular to the Sun-facing deck of the ACE spacecraft. While the ACE design goal is for the spin axis to be perpendicular to this deck to within 0.5°, the exact orientation will not be known until after deployment of the solar panels on orbit.

Ions entering the ESA at different polar angles with respect to the aperture normal end up being counted in different CEMs, thus identifying the incident polar angle of the ion in the plane of the acceptance fan of the instrument. As ACE spins, the CEMs sweep out small conical segments of the sky, centered on the spacecraft spin axis direction. The combination of CEM identification and spin phase of the spacecraft provide unique directional information about all ions measured in the instrument. Further, the high voltage step of the ESA selects the E/q of transmitted ions. This combination of CEM number, spin phase, and ESA step level, which is equivalent to polar angle, azimuthal angle, and energy of the incident ions, respectively, provides the basic matrix of measurements in which SWEPAM-I counts are collected.

SWEPAM-I instrument capabilities and hardware parameters are summarized in Tables II and III, respectively. This instrument makes full 3-D plasma measurements of protons and alpha particles every 64 s. In its search mode (typically once every 32 minutes) SWEPAM-I covers the entire 260 eV q^{-1}–36 keV q^{-1} energy range. Between search modes, SWEPAM-I tracks the solar wind and measures every other of 40 energy levels around the peak; track mode provides 5% energy resolution measurements every 64 s. In addition, observations from two adjacent

TABLE II
SWEPAM instrument capabilities

	SWEPAM-I	SWEPAM-E
Particle species measured	3-D protons and alphas	3-D electrons
Energy range	260 eV/q–36 keV/q	1.6 eV–1350 eV
Energy resolution $\Delta E/E$ (FWHM)	5% or 2.5% (1)	12%
Analyzer K (ion energy/ESA voltage)	17.1	4.3
Polar angle FOV	(−)25° to 65°	10°–170°
Polar angle resolution (FWHM)	5° or 2.5° (2)	21°
Azimuthal angle resolution (FWHM)	3° to 4.5° (3)	9° to 28° (3)
G-factor/pixel (cm^2 sr eV/eV)	$1–20 \times 10^{-6}$	$2–7 \times 10^{-4}$
Time resolution	64 s	64 s

(1) 2.5% for energy interleaved data (128 s resolution).
(2) 2.5° if orientation of S/C spin axis allows interleaving data from both sides of fan.
(3) Smaller angles are for normal incidence; larger angles are at the maximum polar ranges.

track modes can be interleaved to give 2.5% energy resolution with 128 s cadence. Section 5 describes the modes of operation in more detail.

Figure 11 displays a photograph of the SWEPAM-I instrument which mounts on the sunward-facing instrument platform of the ACE spacecraft. The instrument is comprised of two major subassemblies, a large cylindrical ‘sensor’ assembly, and a rectangular ‘electronics box’. The two are joined by angled mounting brackets, which set the pointing angle of the sensor head and, hence, instrument aperture with respect to the spacecraft spin axis.

3.1. SWEPAM-I SENSOR

Components of the ion sensor are housed in the ribbed, thin-walled, drum-shaped container visible in Figure 11. All of the parts are attached to the end covers of the drum. The curved-plate electrostatic analyzer is mounted on the inside of the sunward drum face, and views space through a single, oversized entrance aperture. The ESA is composed of nested spherical section plates having a 105° bending angle. Conically-shaped stiffening ribs were machined as integral parts of the curved aluminum alloy plates in order to maintain their dimensional stability. Both of the plates were coated with copper and blackened using an Ebanol-C process in order to reduce UV scattering into the sensor. The electrostatic analyzer has a gap width of 2.84 mm between plates and an average radius of 100 mm.

Sixteen channel electron multiplier detectors, or CEMs, are arrayed such that their 7 mm funnels have 5° polar angle separations around the edge of the gap where the particles exit the analyzer plates. Each is individually mounted on a ceramic card which also carries glass-coated thin film resistors and bare ceramic

TABLE III
SWEPAM hardware parameters

	SWEPAM-I	SWEPAM-E
Box size (L × W × H) (cm)	36 × 24 × 30	25 × 18 × 19
Mass (kg)	3.7	2.5
Power, average (W)	3.1	2.7
Power, peak (W)	3.3	2.9
Telemetry rate (b/s)	540	460
Number of CEMs	16	7
Temperature limits (°C)		
Preferred operating	0 to +20	0 to +20
In calibration	−20 to +45	−20 to +45
Operating survival	−25 to +50	−25 to +50
Non-operating survival	−30 to +60	−30 to +60
EMC interference		
DC magnetic	0.01 nT @ 10′	0.03 nT @ 10′
AC magnetic	BDL	BDL
AC electrical	BDL	BDL
Ordnance	2 dimple motors	2 dimple motors
Red tags (HV safe/arm)	2	2

BDL: Below Detectable Levels.

coupling capacitors needed to bias the anode slightly positive with respect to the exit end of the CEM, and to couple out the signal. This arrangement maintains cleanliness in order to guarantee long CEM lifetimes (e.g., McComas and Bame, 1984 and references therein), permits replacement of individual CEMs as needed, and enables the precise spacing that is required for the fine angular resolution of this instrument.

In the twin instrument on the continuing *Ulysses* mission, a motor-actuated aperture wheel provides the variable sensitivity required to make measurements across the wide range of heliocentric distances covered by that mission. For ACE, which remains at a fixed distance of 0.99 AU, this mechanism was replaced with a single, oversized entrance aperture wide enough to expose the entire width of the analyzer gap, and extending 7.8 mm along the gap. The aperture is covered with a simple, spring-loaded dust cover. Redundant pyro-activated dimple motors actuate the release mechanism by command, on orbit.

The ACE mission limits the Sun-spacecraft spin axis angle to between 4° and 20°, far less than the *Ulysses* mission. Therefore, we were able to build new instru-

Figure 11. Photograph of the SWEPAM-I instrument. The large cylindrical housing is the sensor head; the rectangular electronics box behind it houses the high and low voltage power supplies and control electronics.

ment mounting brackets, visible in Figure 11, that are configured so that, when the instrument is mounted on the spacecraft, rotation of CEMs 1-12 about the spin axis covers the total angular range of solar wind ions expected throughout the mission. The central axis of the measurement array, parallel to the spacecraft spin axis, is located one quarter of the way between the centroids of CEMs 5 and 6 ($\theta = 18.75°$).

The new mounting scheme also makes it possible to devote four of the SWEPAM-I polar angle detectors to high-sensitivity measurements of suprathermal ions. We therefore added a thin aluminum exit aperture mask covered with 70 lines per inch, 92% transmissive nickel mesh interposed between the exit of the analyzer plates and the CEMs. This mesh, biased at the same voltage as the funnels, precludes electric fields from the ESA from reaching into the funnels and affecting the CEM counting efficiencies. This mask also provides two different sizes of exit apertures. Analyzed ions enter funnels 1–12 through apertures tailored for solar wind ion fluxes near 1 AU. These apertures are 0.4 mm wide, selecting ions exiting only from the very center of the gap. CEM funnels 13–16, which will be exposed only to suprathermal ions and not to the solar wind ion beam because of their angular positions, have circular apertures in the exit mask large enough to transmit ions from across the ESA gap into the CEM funnels.

Each of the sixteen CEMs is connected to its own dedicated amplifier-discriminator circuit on its own miniature printed circuit board, located on the outside of the sensor box. Signal lines are fully shielded, only a few centimeters long, and pass through the sensor box wall on individual miniature feedthroughs, in order to avoid any cross-talk or noise pickup at the inputs to these sensitive circuits. These circuits amplify and discriminate pulses from the CEMs; each discriminator has two, selectable level settings of 1×10^6 and 2×10^7 electrons per pulse. The lower, more sensitive setting is used for all science observations while a combination of alternating between these levels and stepping the CEM high voltage is used for periodic CEM gain calibrations. Normalized pulses from the 16 circuits are cabled to counters in the electronics box.

Since the pumping speed through the aperture is small, SWEPAM-I is fitted with an additional pump-out baffle box to enhance the evacuation of the interior of the instrument. The blackened baffle box requires a minimum of seven surface reflections between its two open ends. This design, fully proven on *Ulysses*, does not allow for any appreciable background from photons or charged particles entering through the pump-out channel. To preserve the cleanliness of the sensor interior, the aperture and baffle openings were hermetically sealed during the long storage period after *Ulysses* development was completed. For the bulk of the ACE spacecraft testing the instrument has been continuously purged.

3.2. SWEPAM-I ELECTRONICS

With the exception of the sensor-assembly amplifier-discriminator circuits described above, the ion instrument's electronics are housed in the attached electronics box (Figure 11). The purpose of the support electronics is to (1) furnish programmed high voltages for the analyzer which sets the ion energy per charge passband, (2) bias the CEMs at commandable high voltages appropriate to achieve high and stable counting efficiency, (3) condition and provide low voltage power for the various electronic circuits and high voltage power supplies, and (4) process and accumulate pulses to form a digitized data string for input into the spacecraft command and data handling system. Figure 12 provides a block diagram of the SWEPAM-I electronics.

In order to configure the *Ulysses* SWOOPS instruments for use on ACE, two fundamental changes were required. First, the instrument's *Ulysses* interfaces needed to be adapted to the ACE spacecraft. Second, the flight processing capabilities needed to be increased in order to meet the ACE science objectives. In order to achieve these objectives, we took advantage of the instrument's modular design and replaced a select number of logic modules and the back plane (motherboard), leaving the heritage high voltage and low voltage supplies untouched.

The electronics box has four cavities: the low voltage power supply, high voltage power supply, motherboard and main electronics cavities. The motherboard cavity is the primary wiring cavity, interconnecting the spacecraft interface con-

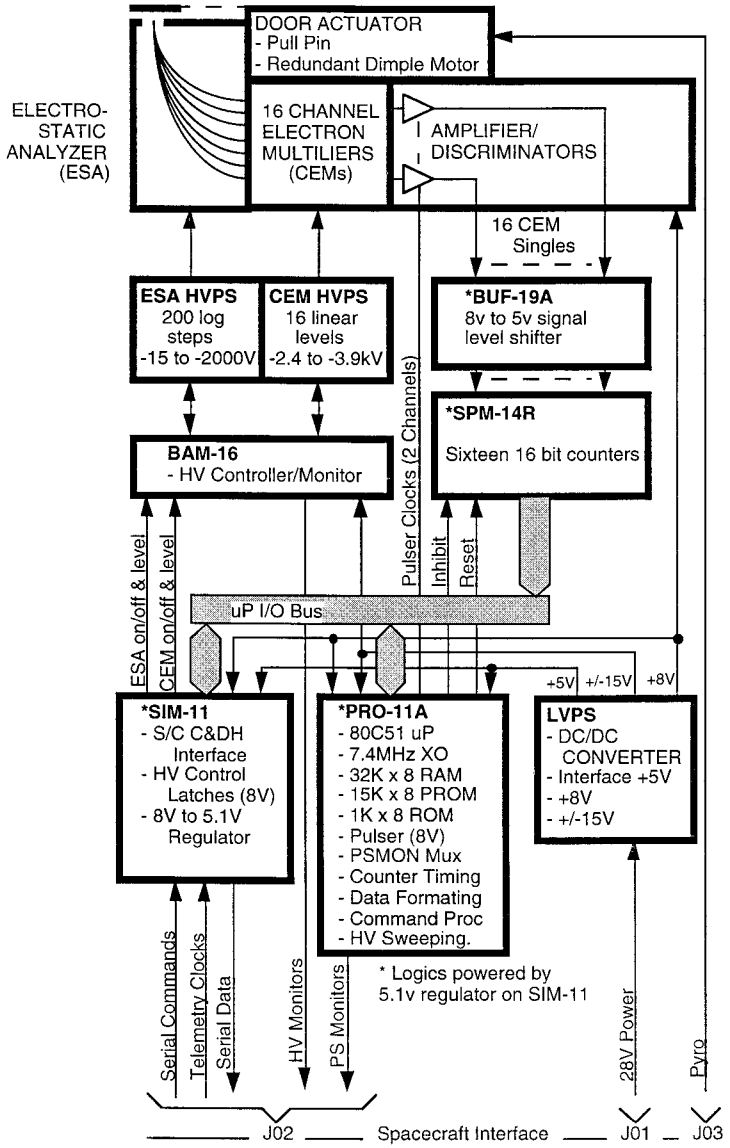

Figure 12. Block diagram of the SWEPAM-I electronics.

nectors, power supplies, processing electronics and sensor electronics. All signals enter and exit this cavity on connectors. The main electronics cavity (tall, central portion of the electronics box) contains five boards or modules: the processor (PRO-11), counters (SPM-14), signal buffer/level-shifter module (BUF-19), spacecraft interface (SIM-11), and high voltage controller (BAM-16) module.

The combined ion instrument has four external connectors: spacecraft command and data handling, spacecraft power, pyro for cover actuation, and a test connector.

The first three are mated into the spacecraft wire harness while the latter is used for test purposes only. SWEPAM-I has two grounds. Signal ground is isolated from the electronics box housing but connected to the electrically isolated sensor head. The signal ground is carried back to the spacecraft single point ground on a wire in the spacecraft harness. SWEPAM-I dissipates 3.1 W when it is fully functional at expected count rates. There are no survival heaters but the instrument is thermally bonded to the thermally controlled spacecraft structure. The instrument temperature is monitored by a sensor mounted on the bulkhead between the motherboard and the low voltage power supply.

3.2.1. *Power Supplies and Controller*

The SWEPAM-I electronics box connects directly to the spacecraft 28 V power and contains both low and high voltage power supplies to produce and condition voltages used in the instrument. Two boards make up the low voltage power supply. The first is a DC/DC converter which isolates the spacecraft primary power ground from the instrument's secondary power ground. This heritage supply 'chopper' was designed to be synchronized to *Ulysses*' power system. The ACE spacecraft does not have power system synchronization so this supply free runs at 55 ± 0.5 kHz. The second board of the low voltage supply rectifies, regulates and filters the outputs from the multi-tap isolation transformer. Spacecraft interface signal line drivers and receivers are powered by $+5$ V; ± 15 V is provided for the high voltage control module and used to condition analog telemetry signals output to the spacecraft; $+8$ V is provided for the sensor amplifier-discriminator circuits; the balance of the processing electronics are powered by an 8 V to 5 V linear power regulator on the spacecraft interface module.

Two encapsulated high voltage supplies are provided: a -2.4 kV to -3.9 kV CEM bias supply and a -15 V to -2 kV electrostatic analyzer field supply. Both supplies are driven by the BAM-16 module. The high voltage supply lines are shielded, coaxial cables; the supply return current is carried on the shield. The CEM bias supply assembly includes the feedback controlled drive circuit, drive current monitor, step-up transformer, five-stage diode/capacitor voltage multiplier and the high voltage monitor/feedback resistor divider network which supplies the reference level for the feedback controller. The ESA field supply assembly includes the feedback controlled drive circuit, drive current monitor, step-up transformer, five stage diode/capacitor voltage multiplier, feedback controlled high voltage shunt regulator and a regulator performance monitor. In order to improve efficiency, this supply is designed to vary both the feedback controlled multiplier and regulator references such that the multiplier output is 10% above the regulator output. Most of this 10% head room is required to allow for the multipliers' slow recovery rate in the 'flyback' to start the next sweep. It turned out that the CEM and ESA high voltage supplies did not function well at the 55 kHz free running power supply chopper frequency; consequently, it was decided to allow these clocks to free run

at their natural frequency (57 kHz) so none of the power supplies are synchronized to the spacecraft power system or to each other.

The BAM-16 high voltage control module provides the supplies with switched input power, drive clocks, reference levels, monitor conditioning and over-current protection. Each supply is activated by its own ON/OFF control signal; an over-current condition will turn this switch off requiring the ON/OFF control signals to be cycled to reactivate the supplies. The processor selects the desired CEM bias level with a four bit control word. The BAM-16 translates this into 16 equally spaced levels from -2.4 kV to -3.9 kV (100 V spacing). The processor also selects the desired ESA field level with an eight bit control word. The BAM-16 translates this into 256 logarithmically spaced levels of which only the first 200 (-15 V to -2 kV) are used.

3.2.2. *Counters, Processor, and Interface Modules*

The SWOOPS digital electronics were all powered with 8 V. It was not uncommon in the late 1970s and early 1980s when the SWOOPS instruments were developed to find CMOS processors, memories and peripherals that would operate at these or even higher levels. By the 1990s when the retrofit of the SWOOPS to the SWEPAM was made, essentially all CMOS had been standardized to run on 5 V. In order to reuse the heritage counter module (SPM-14), a new module (BUF-19) was added to level shift the 8 V amplifier-discriminator signals to 5 V level before routing to the counter module. The SPM-14 module contains 16 counters, one per CEM, and the bus interface circuits. The TA585 counters used are custom 16-bit counters which interface directly to an eight bit processor bus. While these devices do not have a spill flag, the SWEPAM sample intervals and electronic count rates preclude an overflow.

The *Ulysses* 1802 microprocessor-based processor module and two memory modules were replaced with a single new processor module, PRO-11. PRO-11 includes an 80C51 microcontroller, 7.4 MHz crystal controlled clock, 2K Bootstrap PROM, 28K EEPROM , 48K RAM, watchdog timer, inflight calibration pulser and an 8 channel power supply monitor multiplexer. The timer, pulser, multiplexer controller, memory controller and I/O decoding are all implemented in a single Field Programmable Gate Array (FPGA).

Using lookup tables, the spacecraft telemetry clock (not the spin clock) and its own chip counter/timer circuit, the microcontroller generates a timing function which sequentially disables the counter inputs, commands a new ESA level, moves the data from the counters into RAM, clears the counters, allows high voltage to settle then re-enables the counter inputs to collect data at the new E/q level. Each instrument data mode has a lookup table which defines the mode in terms of the E/q level and count interval, high voltage settling times, number of E/q levels per spin sector, number of spin sectors per spectral segment (roughly equivalent to a spin) and the number of spectral segments per mode.

Bootstrap PROMs contain the firmware which initialize the instrument when the processor is first activated and provide the facilities to load all flight software into EEPROM or RAM. These devices are read-only and contain two copies of the bootstrap codes to ensure there is always a way to correct or tune the flight software. The EEPROMs contain the bulk of the flight software. The instrument will be launched with the most current version of the flight software resident in the EEPROM. If any software uploads are required after launch, they will most likely be limited to revisions of the data mode lookup tables that are moved to RAM by the startup codes.

To accommodate these instruments on the ACE spacecraft, a new spacecraft interface module was designed to replace the *Ulysses* heritage interface. This module, the SIM-11, includes the command receiver, framing pulse receiver, data transmitter, high voltage control latches (CEM and ESA ON/OFF, CEM Level and ESA Level) and an 8 V to 5 V linear power regulator to supply the processor electronics. In order to keep the number of processor interrupts to a minimum, the data transmitter uses a first-in/first-out (FIFO) memory device permitting the processor to buffer an entire minor frame's worth of data between readouts. Except for this FIFO and the linear regulator, all functions on this module are implemented in a single FPGA.

3.3. SWEPAM-I CALIBRATION

Calibration of SWEPAM-I was performed at the Los Alamos plasma analyzer calibration facility. The angular and energy response functions for all sixteen CEMs were measured using a known, unidirectional, 5 kV proton beam. In order to maintain absolute cleanliness for the CEMs during the calibration, we chose to mount only the cylindrical sensor head, and not the electronics box, within the vacuum chamber. The sensor head was mounted on a computer-controlled three-axis table (two orthogonal rotation stages and one translation stage) which allowed ions to be directed at the aperture over all possible input angles for the instrument. A 3-dimensional array of sensor transmission/counting efficiencies was obtained as a function of polar angle, azimuth angle, and ESA voltage (giving E/q) for each CEM. The response function of the instrument is completely defined by these sixteen 3-dimensional arrays.

An example of a 2-dimensional cut through the 3-dimensional response function is shown for CEM 4 in Figure 13. Levels of transmitted ions from an ion beam arriving at a fixed 20° polar angle are color coded as a function of azimuthal angle and ESA voltage. The azimuthal and energy responses are coupled as expected for a spherical section electrostatic analyzer (Gosling et al., 1978); the polar response is essentially decoupled from these two. Figure 14 shows three 1-dimensional cuts through the response function for channel 4 at the centroids of each of the other two parameters. In each, the measured number of counts (solid line) is fit with a theoretical curve (dotted line). In Figure 14(a) the distribution of counts for CEM

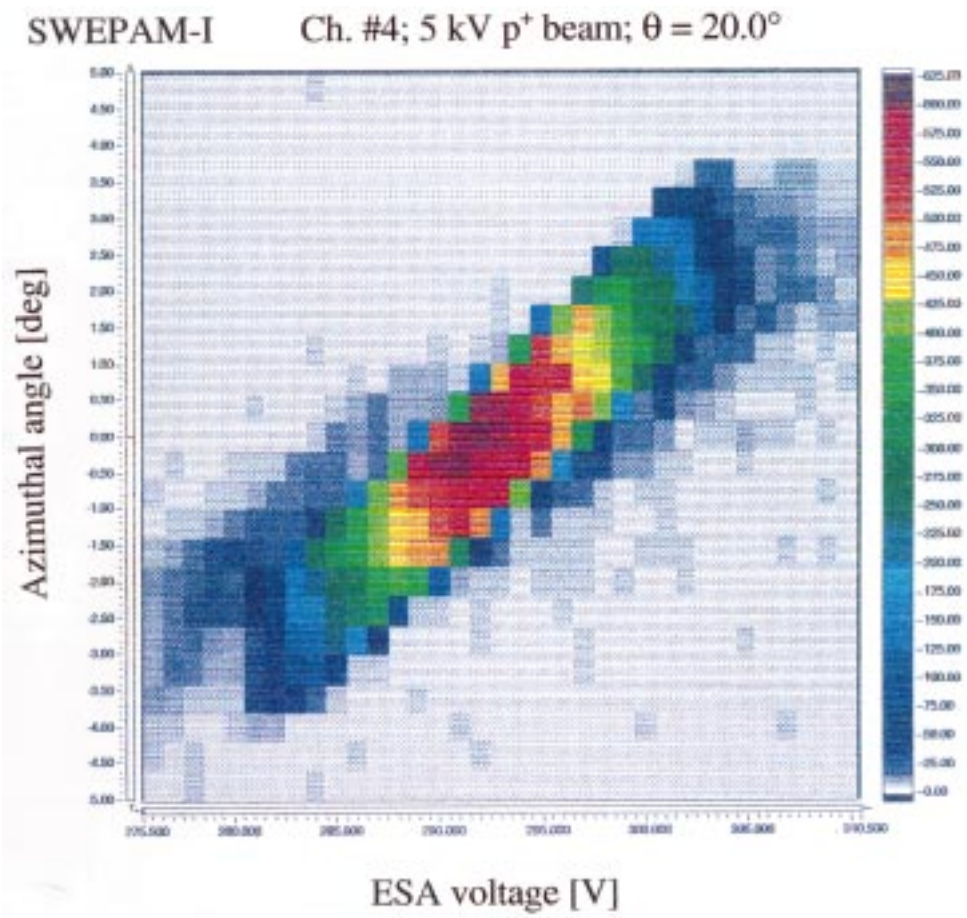

Figure 13. Color-coded plot of transmitted counts through channel 4 of SWEPAM-I as a function of azimuthal angle and ESA voltage (equivalent to E/q) for a 5 kV proton beam incident at a polar angle of 20°.

4 is shown as a function of analyzer plate voltage for the 5 keV proton beam in a look direction given by $\phi = 0°$ and $\theta = 25.8°$. The response is approximated by a gaussian profile. The azimuthal profile of the CEM at an analyzer plate voltage of 293 V and polar angle of $\theta = 25.8°$ is also approximated by a gaussian profile and is shown in Figure 14(b). While the responses as a function of both analyzer plate voltage and azimuth are approximated by a gaussian, the response in polar angle is best approximated by a trapezoid. Comparison of the measured counts with the best-fit trapezoid is shown in Figure 14(c) for an azimuthal angle of 0° and analyzer plate voltage of 293 V. The measured analyzer constant for SWEPAM-I, given by the ratio of incident particle energy to plate voltage, is ∼17.1.

Calibration data similar to those shown for CEM 4 were taken for each of the 16 CEMs in SWEPAM-I. Figure 15 shows a polar cut through all 16 channels at

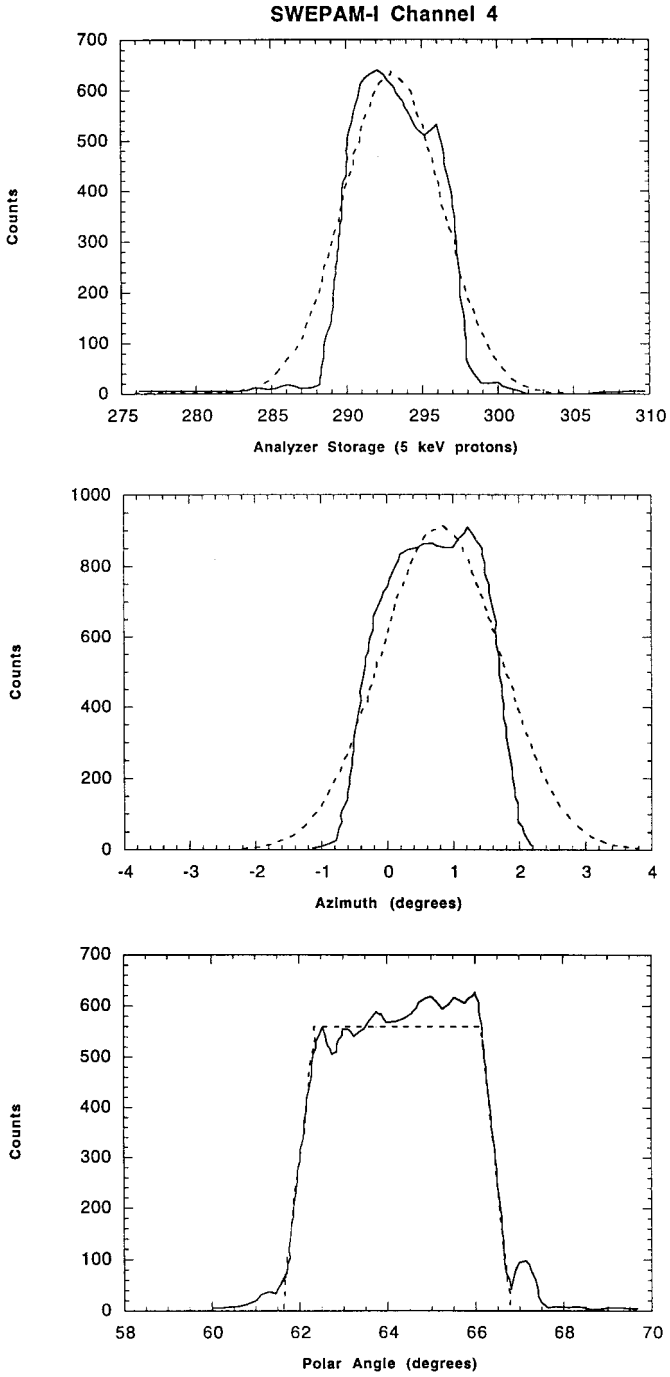

Figure 14. Central energy (a), azimuthal angle (b), and polar angular (c) cuts through the channel 4 response function of SWEPAM-I. The solid lines show the calibration data while the dotted curves display theoretical fits.

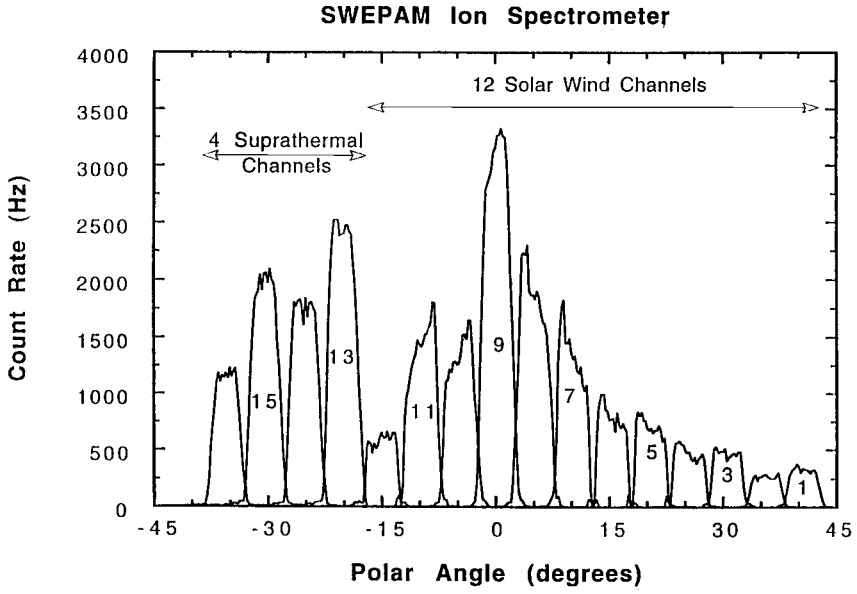

Figure 15. Polar angular cut through all 16 channels of SWEPAM-I at 0° azimuth and the peak of the E/q transmission curve. The four unmasked, suprathermal channels have appreciably larger transmission than they otherwise would for such large polar angles.

0° azimuth. This cut appears to be more variable than one might have expected, however, multiple runs confirmed the variations shown. In addition, the roughness of these curves is at least in part attributable to the fact that the central azimuth was slightly different ($<1°$) for each channel and that the very narrow angular response functions were cut in slightly different places. In any case, the full response function information is used in characterizing each channel's calibration curves.

Once these 16 arrays were fully measured, the polar, azimuthal, and energy responses were characterized and the geometric factors for each CEM were calculated. Geometric factors were calculated by numerical integration of the three response functions (energy, θ-angle, and ϕ-angle) over all energies, and all angles. These geometric factors provide the necessary conversion from the measured counts to more physically meaningful distribution functions, from which one can calculate the moments of the distribution such as density, flow velocity vector, temperature matrix, and the heat flux. Table IV summarizes the calibrated geometric factors for SWEPAM-I.

4. Solar Wind Electron Instrument (SWEPAM-E)

Like SWEPAM-I, the electro-optical design of the solar wind electron instrument, SWEPAM-E, is based around a spherical section electrostatic analyzer. For SWEPAM-E, the bending angle of the analyzer is 120°. Figure 16 schematically

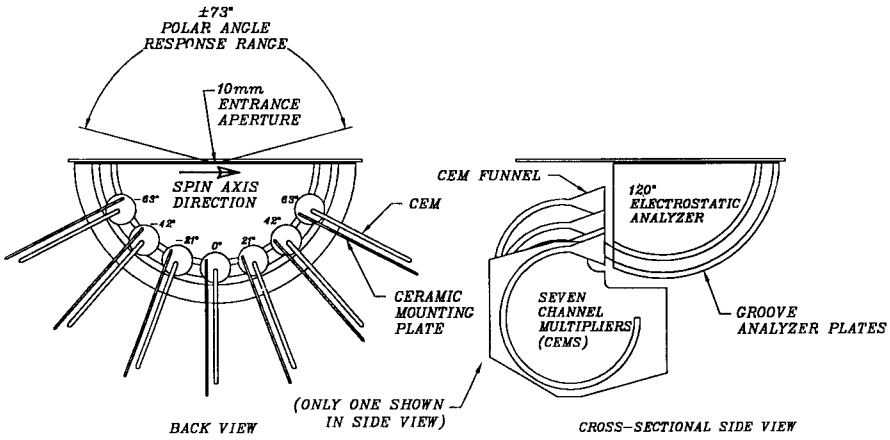

Figure 16. Schematic diagram of the SWEPAM-E electro-optics, similar to Figure 10.

TABLE IV

Geometric factors for SWEPAM (10^{-6} cm^2 sr eV eV^{-1})

CEM	G	CEM	G	CEM	G	CEM	G
1	7.62	5	8.50	9	0.92	13*	16.67
2	7.42	6	6.01	10	1.59	14*	15.20
3	9.23	7	5.07	11	2.86	15*	20.77
4	8.67	8	1.63	12	4.69	16*	14.88

* Used for measuring suprathermal instead of solar wind ions.

displays the SWEPAM-E electro-optics. Electrons enter the instrument through its aperture which is pointed normal to the spacecraft spin axis. A positive high voltage on the inner plate of the ESA biases the analyzer such that only electrons within a range of energies (12%) and azimuthal angles (9° at $\theta = 0°$ to 28° at $\theta = \pm 70°$) are permitted to pass through the analyzer and are detected in the seven channel electron multipliers (CEMs) located immediately behind the analyzer.

Polar and azimuthal angles are defined just as they were for SWEPAM-I. Electrons entering the ESA at different polar angles with respect to the aperture normal end up being counted in one of the seven CEMs which gives 21° polar angular resolution for electrons entering in the wide azimuthal angle, fan-shaped field-of-view (FOV). The plane of symmetry of the fan is parallel to the spacecraft spin axis and the middle CEM (#4) viewing angle is centered on a plane parallel to the spacecraft equator ($\theta = 90°$). As ACE spins, the SWEPAM-E fan-shaped field-of-view sweeps out >95% of 4π sr, missing only small ($\sim$10° half angle) conical

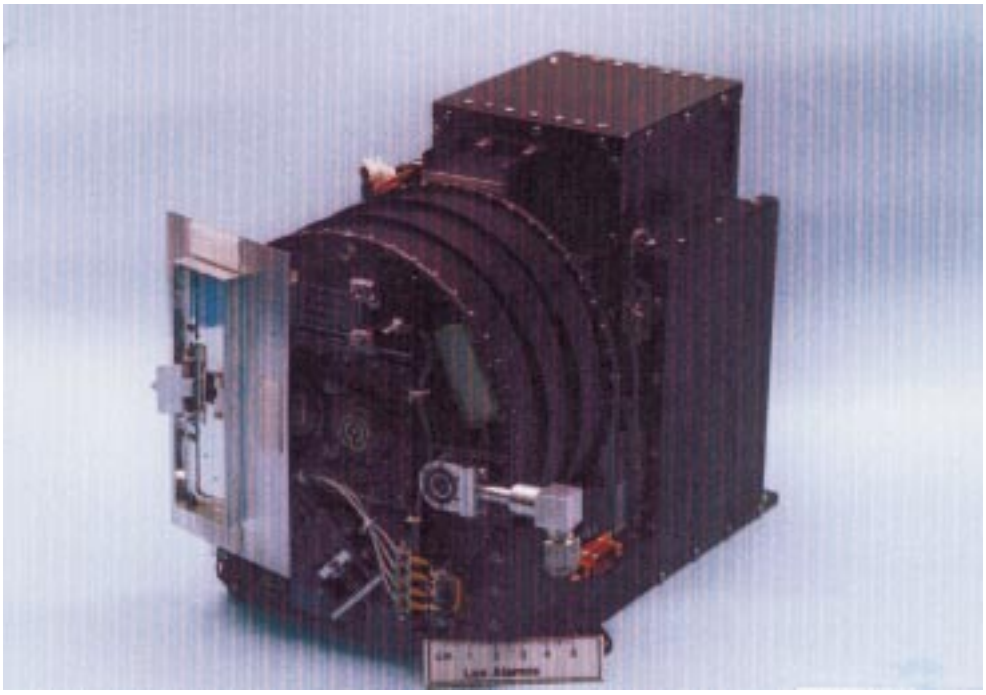

Figure 17. Photograph of SWEPAM-E; similar to Figure 11.

holes centered along directions parallel and anti-parallel to the spin axis (roughly along the radial direction to and from the Sun). Electrons with energies from 1.6 eV–1.35 keV are measured in 20 contiguous energy bins determined by the instrument's high voltage stepping. Again, the combination of CEM number, spin phase, and ESA step level, which is equivalent to polar angle, azimuthal angle, and energy of the incident electrons, respectively, provides the basic SWEPAM-E measurement matrix. The general SWEPAM-E instrument and hardware parameters are summarized in Tables II and III, respectively.

Figure 17 displays a photograph of the SWEPAM-E instrument which also mounts on the sunward-facing instrument platform of the ACE spacecraft. Like SWEPAM-I, this instrument is comprised of two major subassemblies, a ribbed, thin-walled, cylindrical sensor assembly, and a roughly rectangular electronics box. The sensor cylinder mounts directly onto an extension of the electronics box such that the instrument aperture points at right angles to the spacecraft spin axis.

4.1. SWEPAM-E SENSOR

The curved-plate electrostatic analyzer is mounted on the inside of the outward pointing drum face, and views space through a single, rectangular entrance aperture. The analyzer is composed of nested 120° spherical section plates of aluminum alloy that are grooved in addition to being blackened in order to minimize

backgrounds caused by UV scattering through the plates and photoelectron and secondary electron production in the plates themselves. The electrostatic analyzer plate system has a gap width of 3.5 mm and an average radius of 41.9 mm. Seven large-funnel (11 mm diameter) CEMs are arrayed with 21° separations along the analyzer plate's exit. A thin aluminum exit aperture mask covered with 70 lines per inch, 92% transmissive nickel mesh (not shown in the simplified drawing) is again interposed between the analyzer exit and CEM funnels to preclude electric fields from affecting the CEM counting efficiencies. Each CEM is mounted on its own ceramic card which also carries the resistors and coupling capacitors needed to bias the anodes slightly positive with respect to the exit of the CEMs and to couple out the signals. Just as for SWEPAM-I, this arrangement maintains cleanliness, permits replacement of individual CEMs as needed, and enables the precise spacing that is required for the fine angular resolution of this instrument. Each of the seven CEMs is connected to its own dedicated amplifier-discriminator circuit; these circuit boards are identical to those used for SWEPAM-I.

Electrons enter the analyzer through an entrance aperture which is wider than the analyzer gap and runs 10 mm along it. At launch, this aperture is also covered with a spring-loaded dust cover to protect the CEMs from contamination. Redundant pyro-activated dimple motors release a mechanism by command on orbit, and allow the cover to be retracted from over the aperture. A blackened pump-out baffle box, similar to the one used on SWEPAM-I, is provided to enhance the evacuation of the interior of the instrument. Throughout most of the observatory level testing SWEPAM-E was also under continuous purge.

Because of the sensitivity of low-energy electrons to spacecraft surface charges, the SWEPAM-E requires a special spacecraft thermal blanket. This blanket maintains the thermal characteristics of the spacecraft, is conductive to carry off any surface charge build-up to the spacecraft bus, and also produces no magnetic field. The side of the SWEPAM-E cover containing the aperture is made with an outer surface of indium/tin oxide (ITO) coated Kapton. This material has the same thermal properties as the regular spacecraft blanket (which is made of beta cloth – a fiberglass material with a Teflon coating). A short ($\sim$25 cm) vertical section of the blanket covering the spacecraft panel below the SWEPAM-E aperture is also made of this ITO coated material. Finally, the original (non-conductive) thermal material on the spacecraft radiator near SWEPAM-E was removed and replaced by a conductive ITO coated silver/Teflon film.

4.2. SWEPAM-E ELECTRONICS

The electron instrument electronics perform the same functions and have a significant amount of commonality with those of the ion instrument. In particular, we determined that it was most cost effective to use a single design for the new electronics hardware for the two instruments. Since the ion instrument's processing requirements were more demanding, they drove the processing and memory

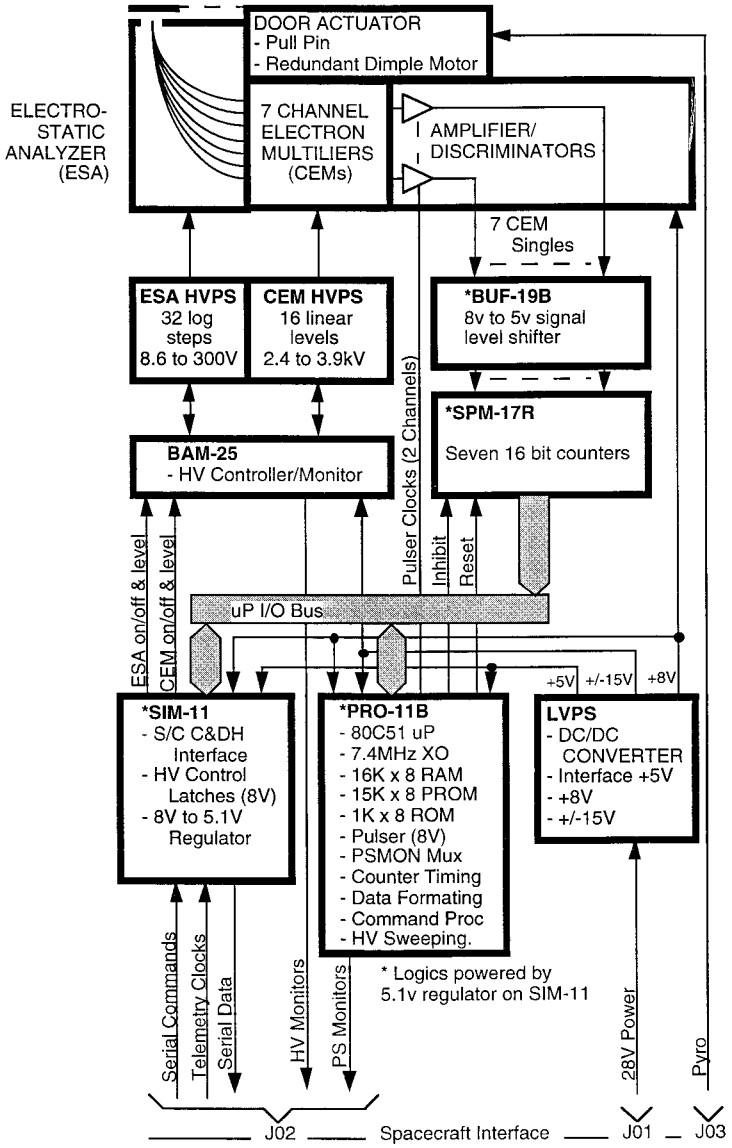

Figure 18. Block diagram of the SWEPAM-E electronics.

resources built into SWEPAM-E as well as SWEPAM-I. SWEPAM-E dissipates 2.7 W when it is fully functional at expected count rates. Its thermal interface is the same as the ion instrument's interface: no heaters, one temperature sensor, and hard mounted to the spacecraft. Figure 18 provides a block diagram of the SWEPAM-E electronics.

This electronics box houses the high and low voltage power supplies, motherboard, wiring, and main electronics. The main electronics cavity contains five

boards or modules: the processor (PRO-11), counters (SPM-17), signal buffer/level-shifter module (BUF-19), spacecraft interface (SIM-11), and high voltage controller (BAM-25) module. Of these, only the SPM-17 and BAM-25 are unique to the electron instrument. The rest of the boards are identical to those used in the ion instrument and described above. SWEPAM-E has the very same four connector interfaces as the ion instrument right down to the pin out and signal ground arrangement with one exception. Since the pyro connector is mounted to the sensor housing rather than the electronics box, its shell is grounded to signal rather than chassis ground. Special precautions were taken to assure that this arrangement did not cause a loss of isolation between the grounds.

While the SWEPAM-E heritage low voltage power supplies are of a different design than those of SWEPAM-I (the SWOOPS ion sensor placed additional requirements on the supply for its aperture stepper motor), they are functionally equivalent, including the same 28 V isolation, free running chopper frequency and secondary powers and grounds. The two encapsulated high voltage supplies are a $+2.4$ kV to $+3.9$ kV CEM bias supply and a $+8.6$ V to $+300$ V electrostatic analyzer field supply. Each supply interfaces identically with the BAM-25 module and sensor head as it did in SWEPAM-I. The CEM bias supply is identical to that of the ion instrument except for output polarity. The ESA field supply assembly is very much like that of the ion instrument except for its voltage range and number of levels. The SWEPAM-E ESA supply output is 32 logarithmic levels from $+8.6$ V to $+300$ V. The first eight levels are not used for the ACE mission. Conversely, in order to extend the top-end range of electron science observations, SWEPAM-E uses the top two levels which were not used by the SWOOPS.

The BAM-25 is the complement of the BAM-16 in the ion instrument and functionally differs only in the number of ESA step levels it controls and its reference levels. In order to get the full range out of this ESA supply, the 1 V reference had to be set slightly low ($\sim$0.9 V) so that the supply would not sag at its highest level. This also decreased the output voltage for all other levels proportionately. Consequently, the SWEPAM-E ESA levels are offset from those on SWOOPS. The SPM-17 counter module is the equivalent to the SPM-14 module in the ion instrument except that it has only seven counters instead of 16. Since the electron instrument did not need as much RAM memory for data buffering, the second RAM chip was omitted during assembly.

4.3. SWEPAM-E CALIBRATION

Calibration of the electron analyzer was performed at the Los Alamos plasma instrument calibration facility in a similar manner to that of the ion instrument. Because our facility produces ions rather than electrons, we chose to also calibrate SWEPAM-E using a 1.05 keV proton beam. This was made possible simply by using a negative high voltage on the inner analyzer plate and using ions with energies well above the several hundred volt post-acceleration bias on the CEM

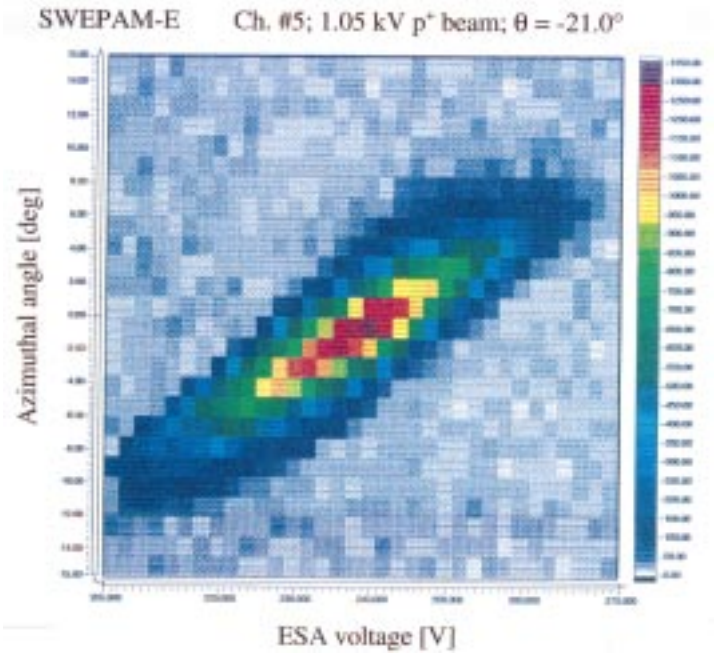

Figure 19. Similar to Figure 13, but for channel 5 of SWEPAM-E, calibrated with a 1.05 kV beam and an incident polar angle of $-21°$.

funnels. This procedure also has some advantages over using electrons as the ions are far less affected by the Earth's magnetic field than are electrons.

The calibration procedure was essentially the same as for the ion instrument. A 2-dimensional (energy/azimuthal) angle cut through the response function for CEM 5, at its polar angle centroid ($-21°$), is shown in Figure 19. Figure 20 displays the central 1-dimensional polar, azimuthal, and energy cuts for this channel in the same format as Figure 14. The distribution of counts for Channel 5 is shown as a function of analyzer plate voltage for 1.05 keV protons in a look direction given by $\phi = 0°$ and $\theta = -21°$ in (a); the central azimuthal and polar response are shown in (b) and (c). Again, the responses in (a) and (b) are approximated by simple gaussians. For electrons, the response in (c) is approximated by a skewed gaussian. Finally, Figure 21 shows the polar cut at 0° azimuth through all seven CEMs in SWEPAM-E. The ratio of electron energy to ESA voltage, or analyzer constant, for SWEPAM-E is ~4.3. The channel-specific geometric factors were derived by the same method as was done for SWEPAM-I and are given in Table V.

Since the SWEPAM instruments, and particularly SWEPAM-E, bear a considerable resemblance to the SWOOPS instruments onboard *Ulysses*, comparisons of calibration results obtained from SWOOPS prior to launch have been made with the SWEPAM calibration; overall the comparison is excellent. As an example, in Figure 22 we compare the geometric factors calculated for the ACE plasma

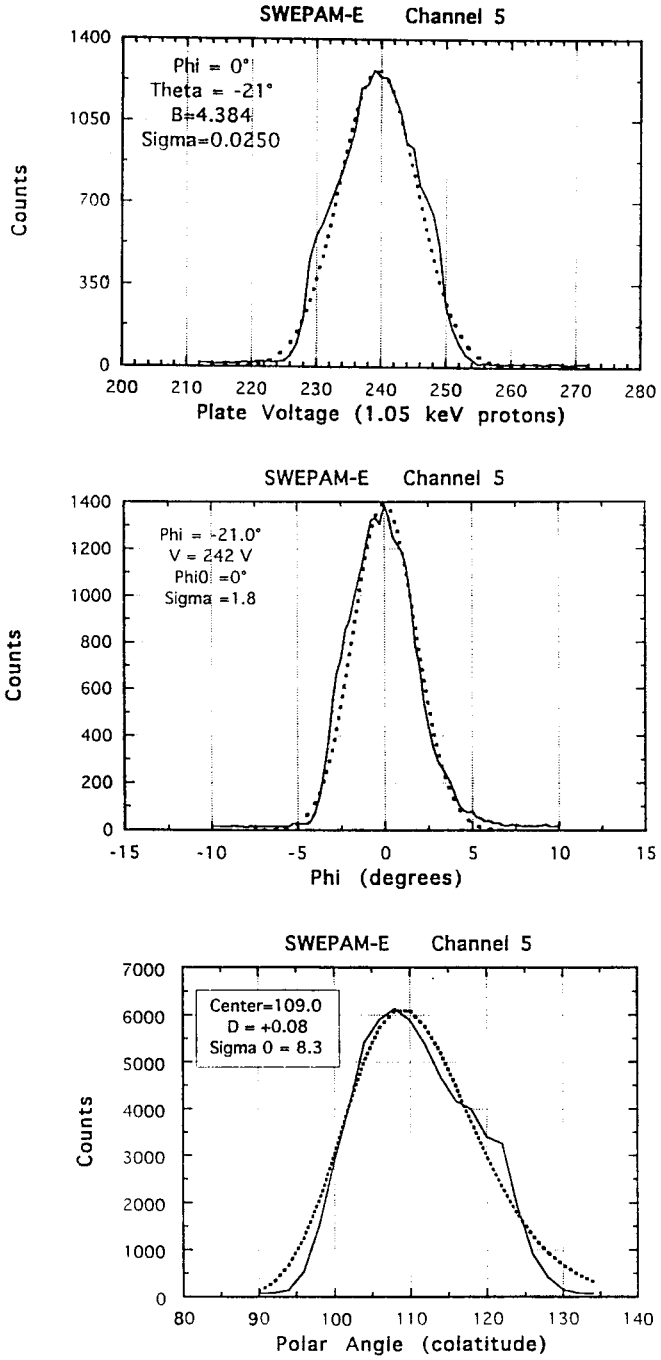

Figure 20. Central energy (a), azimuthal angle (b), and polar angular (c) cuts through the channel 5 response function of SWEPAM-E along with theoretical fits, similar to Figure 14.

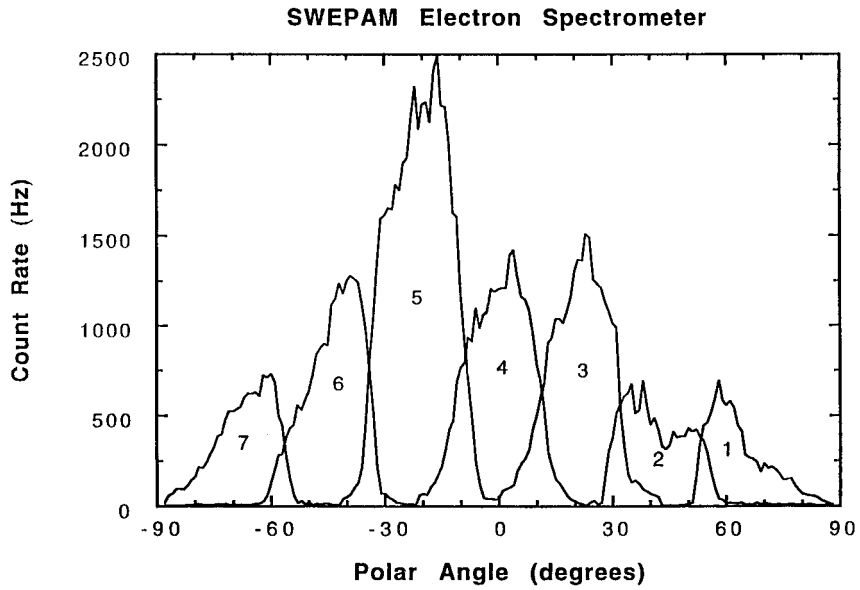

Figure 21. Polar angular cut through all seven channels of SWEPAM-E at 0° azimuth and the peak of the E/q transmission curve, similar to Figure 15.

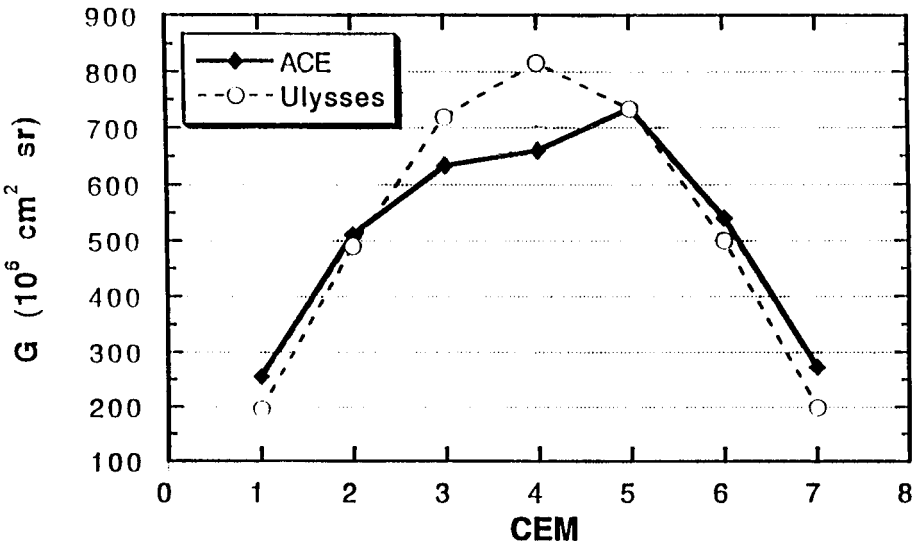

Figure 22. Comparison of SWOOPS and SWEPAM-E geometric factors. The differences in channels 3 and 4 are probably traceable to slight differences in the actual hardware and CEMs.

TABLE V
Geometric factors for SWEPAM-E (10^{-6} cm^2 sr eV eV^{-1})

CEM	G	CEM	G
1	255.6	5	733.5
2	511.0	6	540.3
3	633.4	7	272.9
4	659.5		

instruments with the geometric factors calculated for *Ulysses*. With the exception of CEMs 3 and 4, the efficiencies are very close. The excellent overall quantitative agreement between these curves, measured in different decades in different calibration facilities, provides support for the accuracy of both sets of measurements. Since the ACE instruments are essentially made up of *Ulysses* spare parts, the flattening of the geometric factor at CEMs 3 and 4 is probably due to differences in the sensor hardware and/or CEMs. Nevertheless, such differences are minor and should not impact the science.

5. Instrument Operations and Data Handling

Owing to the large differences between the *Ulysses* and ACE orbits, as well as the large leaps forward in computing capability over the years between the two instruments' development phases, the SWEPAM data modes and operations have been completely reworked. As such, this section describes a completely new development for the ACE program. Several of the features of the new operations allow SWEPAM-I and SWEPAM-E to provide substantially improved data products over their *Ulysses* counterparts.

Throughout this section we will use the term 'cycle' to describe the top-level instrument process. Cycles are comprised of sequences of 'modes' which are further comprised of sequences of 'segments' which occur over intervals that are roughly equivalent to the spacecraft spin period. The nominal ACE spin rate is 5 rpm or 12 s per spin. Operation of SWEPAM is synchronized with the telemetry rate. This choice yields a nominal data accumulation period (or segment) of 12.8 s which is also just slightly longer than the longest possible spacecraft spin period forecast for the mission (12.2 s). The difference between the actual spin period (which will not be known until after launch, and may change slightly over the course of the mission) and 12.8 s causes the data sampling window to precess around from one spin to the next. As will be described below, this is not a concern because the

SWEPAM microprocessor selects out the most interesting samples in the full data matrix for telemetering.

Table VI summarizes all science data sets for both SWEPAM-I and SWEPAM-E; details are given in the following subsections. The first five products are derived from the ion instrument and the last three are derived from the electron instrument. The data mode from which the data set were derived is shown in column 2. Column 3 provides a brief description of the data set. The fourth column describes the data set matrix in terms of energy (E), polar angle or CEM (θ), and azimuth or spin angle (ϕ). The notation $\theta - \phi$ is used to indicate that a mask has been applied and only a subset of $\theta - \phi$ angles are telemetered. The last column provides the time resolution and cadence for each data product. Thus all science data sets have a basic time resolution of 64 s. The cadences indicated are based on expected data mode cycles, but can be easily changed during the mission.

5.1. COMMANDING AND HOUSEKEEPING

Once the SWEPAM instruments have been powered by the spacecraft, they are operated by two distinct classes of ground commands: hardware commands (hard commands) and software commands (soft commands). Both classes are transmitted to the instruments from flight operations ground computers through the spacecraft as serial data commands. The hard commands are dispatched by a hardware decoder to control critical hardware redundancies and interlocks. The soft commands are dispatched by one of two command processors in the flight software and can either update the EEPROM flight codes and RAM data base or select and control the data acquisition functions. All SWEPAM operational commands are defined in the flight operations data base and are issued from command procedure files which verify the commands and instrument responses. The spacecraft has provisions for stored and autonomous instrument commands. There are currently no plans to use stored commands to operate the SWEPAM instruments. The only autonomously implemented commands for SWEPAM are power shedding if either a spacecraft or instrument power fault is detected.

The SWEPAM instruments each have three housekeeping ‘channels’. The analog telemetry consists of eight low voltage monitors multiplexed on one of the three analog signals and 11 high voltage control monitors multiplexed on two other analog signals. These signals are converted by the spacecraft and provided at a rate of one sample per major frame (i.e., 16 s). Eight major frames are required to collect a full set of these monitors. In addition, housekeeping data are provided in the first 40 bits of each major frame to enable operation and monitoring of the instrument by the flight operations team. Twenty-four bits of this same header are output in the RTSW data link. The header is the key to data set formats, identifying the data set type and frame count. Operating parameters required to interpret the science data are embedded in the science data sets, in data set headers, and spectral segment headers as appropriate.

TABLE VI
SWEPAM science data products

Acronym	Data mode	Species	Description	Data matrix	Time res./ cadence (s)
DSWI	SWI	Ion	Plasma ion velocity distribution	40 (E) × 96 (θ-ϕ)	64/64
DSTI	SWI	Ion	Suprathermal ion velocity distribution	20 (E) × 4 (θ) × 6 (ϕ)	64/64
DSSTI	SSTI	Ion	Plasma ion velocity distribution	40 (E) × 96 (θ-ϕ)	64/1984
DSTI2	SSTI	Ion	Suprathermal ion velocity distribution	20 (E) × 4 (θ) × 6 (ϕ)	64/1984
DRTSW	SWI	Ion	Real time solar wind	40 (E) × 33 (θ-ϕ)	64/64
DNSWE	NSWE	Electron	Plasma electron velocity distribution	20 (E) × 5 (θ) × 30 (ϕ) 2 (θ) × 15 (ϕ)*	64/128
DSTEA	STEA	Electron	Suprathermal electron distribution	10 (E) × 5 (θ) × 60 (ϕ) 2 (θ) × 30 (ϕ)*	64/128
DPHE	PHE	Electron	Photoelectron distribution	20 (E) × 5 (θ) × 30 (ϕ) 2 (θ) × 15 (ϕ)*	64/1984

* First set of angles refers to CEMs 2 through 6. Second set for CEMs 1 and 7.

5.2. ION MODES AND OPERATIONS

SWEPAM-I has four commandable data modes and two commandable data cycles. The data modes are: engineering (ENGI), calibration (CALI), solar wind ion (SWI), and search suprathermal ion (SSTI). Data modes can be run individually or as part of a data cycle. The data cycles are; normal and calibration. The normal cycle is a sequence of one SSTI (search) mode followed, nominally, by 30 SWI (track) modes. The number of SWI modes, and therefore the duration of this cycle, is command adjustable. Once selected, the normal cycle runs continuously until a command is sent to select a new data mode or cycle. The calibration cycle consists of a sequence of two CALI modes to ensure that a change in the solar wind does not corrupt the data set. This cycle will run once after being commanded and then the operation returns to the data cycle (or data mode if no cycle is running) that was in effect at the time the calibration cycle command was received. Except in the event of a 'cycle abort' command, a cycle cannot be interrupted. Therefore, a newly commanded data mode or data cycle will not take effect until the current cycle has completed.

With the exception of the ENGI data mode, which becomes a contingency mode after instrument turn-on and initialization in space, all other modes collect data for four major frames or 64 s. The data collected during this period comprises one full spectrum subdivided into five 12.8 s spectral segments. Since the nominal spin period is 12 s and the worst case predicted spin period is 12.2 s (a 2% error), each spectral segment contains data from slightly more than one complete spin. For all data modes, count accumulation begins at the start of a major frame, and readout of a spectrum begins one major frame later.

Telemetry rate restrictions necessitate the use of several techniques to reduce the number of bits actually transmitted. One of these techniques is a compression algorithm that is used to compress the 16-bit counts and count sums to eight bits. The algorithm, which makes use of a compression table, introduces errors that are typically 1–2% and in the worst case, no larger than 3%.

5.2.1. *Solar Wind Ions (SWI)*

The SWI data mode is often called the 'Track Mode' since it uses the level with the maximum counting rate (L_{mx}) in the previous SWI or SSTI data set to adjust the E/q range of the current collection. Azimuthal angle samples are taken from each of the 16 CEMs (polar angles, θ) at 40 (8 per each of 5 spectral segments) consecutive even or odd E/q levels starting with the level $L_{\mathrm{mx}} - 25$. In a repeating sequence of SWI modes, it is this subtraction of an odd number from the previous L_{mx} that results in the alternating even-numbered/odd-numbered starting energy level. Since the E/q spacing between adjacent levels is 2.5%, every other level corresponds to an E/q spacing of 5%. Thus it is possible to interleave adjacent data sets and provide the highest possible resolution of 2.5% (at the expense of a factor of two in temporal resolution). There are 61 ϕ-angle sectors in a spectral

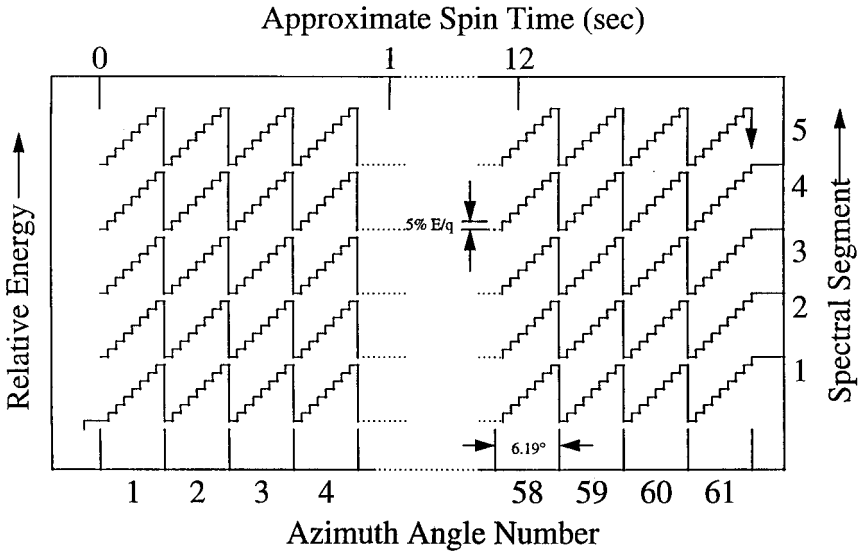

Figure 23. Analyzer plate voltage sequence for SWI (track) mode. Azimuth angle (or spin) is plotted along the x-axis and energy is plotted along the y-axis. Forty levels are stepped through (5 spectral segments $\times$ 8 steps during each ϕ-angle). This subset of 200 possible levels is controlled by continually tracking the proton peak. The stepping sequence for the SSTI (search) mode is qualitatively the same.

segment and at the nominal 5 rpm spin rate the ϕ-angle sectors at a given E/q level are spaced by 6.19° and are 0.59° wide. Since there are 58 ϕ-angles per spin at this nominal spin rate, the SWI mode intentionally over-samples. The sequence of energy level (voltage) stepping is illustrated schematically in Figure 23. Each horizontal profile corresponds to a spectral segment, which is roughly equal to one spin.

The SWI mode produces three data sets. The first (DSWI) consists of counts from CEMs 1 through 12. The second (DSTI) consists of counts from the unmasked CEMs 13 through 16. The third (DRTSW) is a subset of the DSWI data set used for real-time solar wind (see Section 5.4).

For DSWI, the telemetry rate for ACE precludes the transmission of all 732 pixels (12 θ-angles $\times$ 61 ϕ-angles) for each of 40 E/q levels, thus a set of $\theta - \phi$ angle masks have been defined that select those pixel locations which well characterize the solar wind peak and adequately cover the suprathermal wings of the distribution function. There are 12 masks, one for each θ-angle (CEM). The mask used for a given spectral segment is determined by the CEM with the peak count rate during that segment. Briefly, the masks were chosen by calculating the angular offset of each pixel look direction and discarding those pixels with an offset greater than 25° from the peak. Of the remaining pixels, 96 were selected such that the pixels were more finely spaced for smaller angular offsets. Thus the output consists of counts at each of 40 energy levels for the 96 $\theta - \phi$ angle positions which best define the

solar wind beam. Although this represents only 13% of the total number of pixels, tests with simulated data sets (based on measurements by the ion plasma instrument onboard *Ulysses*) indicate that even under extreme solar wind conditions, where the ion beam is extremely broad (i.e., slow and hot), almost none of the non-zero data pixels will end up being discarded by this scheme. As noted above, the SWI mode collects more than one spin's worth of data. The instrument timing function allows for adequate ESA high voltage settling time at the start of each spectral segment and then collects 61 phi-angle sectors. The mask associated with the theta angle with the maximum counts is applied to the first 58 sectors (a command adjustable number to allow for variations in the spin rate) to preclude seeing the solar wind twice in one data set.

Samples from the outer four θ-angles, representing the suprathermal population from CEMs 13 through 16, are presented in the DSTI data set. Again, telemetry restrictions preclude the transmission of the entire array and two averaging procedures are performed onboard. First, the eight E/q levels measured in each spectral segment are summed in pairs to form four E/q levels per spectral segment. Second, the first 60 of the 61 ϕ-angles per pair of E/q levels are further summed to form 6 ϕ-angles per spectral segment. Thus the final DSTI data set contains 29 E/q levels, 4 θ-angles, and 6 ϕ-angles.

5.2.2. *Search/Suprathermal Ions (SSTI)*

During the SSTI mode, a fixed voltage stepping scheme is used with a step interval of 5 at low energies (first two spectral segments) and 4 at higher energies (last three segments). This mode allows construction of a complete suprathermal ion array and enables a robust determination of the solar wind energy peak, L_{mx}, in the event that the peak-tracking is lost during a SWI mode. The resulting energy range covered by these steps ranges from ~500 eV q^{-1} to 35.2 keV q^{-1}. At low energies (segments 1 and 2), the E/q spacing is 12.5% and at higher energies (segments 3–5) the E/q spacing is 10%.

Two data sets are produced from the samples collected in the SSTI mode; DSSTI and DSTI2. These are exactly the same in format as DSWI and DSTI, respectively, although the energy range covered is broader and the energy resolution is less. Thus the DSSTI contains a complete but coarse energy spectrum from 500 eV q^{-1} to 35.2 keV q^{-1}, while DSSTI provides a spectra at about one quarter of the energy resolution of the DSWI mode, but over a much broader range of energies.

5.2.3. *Ion Calibration (CALI)*

The CALI mode allows the determination of the gain saturation level of the CEMs. The E/q level is fixed at the peak of the distribution (L_{mx} level) from the previous search or track mode. The CALI mode data collection consist of 16 CEMs $\times$ 5 CEM bias levels $\times$ 108 ϕ-angles $\times$ 2 threshold levels. The discriminator threshold is alternated between A and B in successive counting intervals of the same ϕ-angle,

with the transition occurring as the counters are read. The operating level of the CEM bias supply (CEMLev) is set by command. During the CALI mode the actual CEM bias level is varied about this operating level for each of the five spectral segments in this sequence; CEMLev−2, CEMLev−1, CEMLev, CEMLev+1 and CEMLev+1.

The data set produced by the CALI mode consists of counts from all 16 CEMs. Again bandwidth restrictions require some averaging of the data. The telemetered data set is created by forming separate sums for the A levels and B levels from four consecutive ϕ-angle sectors. Thus, this data set consists of 16 CEMs $\times$ 5 CEM HV levels $\times$ 2 threshold levels $\times$ 27 ϕ-angle sums.

5.3. Electron Modes and Operations

SWEPAM-E has five commandable data modes and two commandable data cycles. The data modes are: engineering (ENGE), calibration (CALE), normal solar wind electron (NSWE), suprathermal electron angle scan (STEA), and photoelectrons (PHE). Data modes can be run individually or as part of a data cycle. The data cycles are: normal and calibration. The normal cycle is a sequence of 15 alternating NSWE/STEA modes (totaling 30 modes) concluding with a single PHE. The number of NSWE/STEA mode pairs, and therefore the duration of this cycle, is command adjustable. Like the ion, the normal cycle runs continuously once selected. The calibration cycle consists of a sequence of two CALE modes and works in exactly the same way as the ion calibration cycle.

With the exception of the ENGE data mode, all modes collect data for four major frames or 64 s. The data collected during this period comprises one full spectrum subdivided into five 12.8 s spectral segments. As with the ion modes, this data collection interval ensures that each spectral segment covers more than a full spin period and ground analysis software is used to orient the data. A 16 bit to 8 bit count compression algorithm is also implemented as described above. Because SWEPAM-I and -E are run independently, the data modes are not synchronized between the two instruments.

5.3.1. *Solar Wind Electrons (NSWE)*

The analyzer plate voltage for the electron sensor has 32 discrete voltage levels (0–31). The first eight levels (0 to 7) correspond to the photoelectron mode on *Ulysses* and are not used on ACE. The NSWE data mode utilizes the highest twenty of these levels (12 through 31), resulting in electron energy steps centered at 3.2 eV to 1377 eV. During each 12.8 s spectral segment four E/q levels are sampled, at each of 30 ϕ-angles, and for each of the seven CEMs. At the nominal 5 rpm spin rate, angle sectors at a given E/q level are spaced by 12.8° and are 3.0° wide.

The resulting DNSWE data set consists of 20 energy levels at each of 30 ϕ-angles for the innermost five CEMs (2–6) and 15 ϕ-angles for the two outermost (largest polar angle) CEMs (1 and 7). The 15 ϕ-angles of the outer two CEMs

are the result of summing counts from adjacent ϕ-angle sectors after the data collection.

5.3.2. *Suprathermal Electron Angle Scan (STEA)*
The STEA data mode utilizes the highest ten voltage levels (22 through 31) corresponding to electron energies centered at 84 through 1377 eV. During each 12.8 s spectral segment two E/q levels are sampled, at each of 60 ϕ-angles, and for each of the seven CEMs. At the nominal 5 rpm spin rate, angle sectors at a given E/q level are spaced by 6.4° and are 3.0° wide.

The resulting DSTEA data set consists of ten energy levels at each of 60 ϕ-angles for the innermost five CEMs (2–6) and 30 ϕ-angles for the outermost two CEMs (1 and 7). The 30 ϕ-angles of the outer two CEMs are the result of summing counts from adjacent ϕ-angle sectors after the data collection. Comparison of the NSWE and STEA data sets shows how energy resolution and angular resolution are traded off. In the NSWE data set, 20 energy levels are measured, but only 30 ϕ-angles. In the STEA data set, ten energy levels are measured, but the resolution in ϕ is increased by a factor of two. This higher angular resolution is sometimes necessary for resolving narrow electron beams.

5.3.3. *Photoelectrons (PHE)*
This data mode is identical to the NSWE, with the exception that the analyzer plate voltages 8 through 27 are used, corresponding to electron energy steps centered at 0.86 to 429 eV. Thus the PHE mode includes four low energy steps not used in the NSWE mode. The DPHE data set is identical in format to the DNSWE data set.

5.3.4. *Electron Calibration (CALE)*
The CALE data mode performs the same function as the CALI mode performs for SWEPAM-I. In this case the E/q level is fixed on nominally 10 eV electrons. The CALE mode data collection consists of 7 CEMs $\times$ 5 CEM bias levels $\times$ 51 ϕ-angles $\times$ 2 threshold levels. The discriminator threshold is alternated between A and B in successive counting intervals (ϕ-angles). As with SWEPAM-I, the operating level of the CEM bias supply (CEMLev) is set by command but varied around this set point by the CALE data collection routine.

The DCALE data consists of counts from all seven CEMs but unlike SWEPAM-I, no averaging is required. Thus, the telemetered data set consists of 7 CEMs $\times$ 5 CEM bias levels $\times$ 2 threshold levels $\times$ 51 ϕ-angle counts.

5.4. REAL TIME SOLAR WIND

The Real Time Solar Wind (RTSW) data set is intended to provide a rough measure of the solar wind plasma conditions once every 64 s, in real time, to the international space physics community. To complement this, magnetic field vectors from the MAG instrument, as well as low-energy particle data from the EPAM

instrument and high-energy particle data from the SIS instrument are also being provided in real time. By mutual agreement of the ACE project and lead investigators for these four instruments, collection and real-time distribution of these data is being performed by the Space Environment Center (SEC/NOAA) in Boulder. It is anticipated that both plots of current solar wind conditions as well as data sets covering some recent interval of time will be provided via the World Wide Web (see Zwickl et al., this issue). Together, these observations should be very useful for real-time monitoring and prediction purposes and should greatly enhance the nation's ability to predict and monitor the space weather environment near Earth.

The SWEPAM Real Time Solar Wind data set consists of a subset of the DSWI data set. These data are only provided when SWEPAM-I is operating in the SWI mode, and thus will typically provide measurements for 30 out of every 31 data sets. Of the 96 pixels telemetered as the DSWI data set in the ACE Science Format, 33 are used for the ACE RTSW format. All pixels chosen for this purpose have offset angles less then 18°. Since this represents 34% of the total number of telemetered pixels (or 4.4% of the total number of measured pixels) any derived parameters (e.g. density, temperature, speed) must be viewed as incomplete values. While still extremely valuable for monitoring and prediction, these values will not be up to full, scientific analysis and publication purposes. Thus, we advocate the use of a prefix such as 'pseudo-' or 'real-time-' to delineate these parameters from the full density, temperature, and speed parameters. Researchers should contact the SWEPAM science team for complete and properly verified data sets for any scientific purposes.

Acknowledgements

This paper is dedicated to John Paul Glore who developed analog electronics at Los Alamos National Laboratory starting in 1946 and ending with the development of the *Ulysses* solar wind plasma experiments. After retiring, JP continued to help out on SWEPAM, which still contains his amplifier/discriminator circuits, until his death in 1996. The design, development, construction, and testing of space instrumentation can only be carried out with the combined technical expertise and dedication of a substantial team effort; we gratefully acknowledge such critical contributions to SWEPAM from Nancy Baca, Juan Baldonado, Richard Bramlett, Leroy Cope, Randy Edwards, Danny Everett, Paul Glore, Irma Gonzales, Jim Lake, Gerrard Martinez, Ignacio Medina, and Nick Olivas, all at Los Alamos National Laboratory and T. A. Ashlock, J. C. Chavez, J. W. Daniels, T. J. Ellis, K. M. Olsberg, D. O. Smallwood, J. H. Temple, and F. J. Wymer at Sandia National Laboratory. This work was carried out under the auspices of the United States Department of Energy with financial support from the NASA, Advanced Composition Explorer program.

References

Axford, W. I.: 1985, 'The Solar Wind', *Solar Phys.* **100**, 575.

Bame, S. J., Asbridge, J. R., Feldman, W. C., Fenimore, E. E., and Gosling, J. T.: 1979, 'Solar Wind Heavy Ions from Flare-Heated Coronal Plasma', *Solar Phys.* **62**, 179.

Bame, S. J., McComas, D. J., Barraclough, B. L., Phillips, J. L., Sofaly, K. J., Chavez, J. C., Goldstein, B. E., and Sakurai, R. K.: 1992, 'The *Ulysses* Solar Wind Plasma Experiment', *Astron. Astrophys. Suppl. Ser.* **92**, 237.

Barraclough, B. L., Feldman, W. C., Gosling, J. T., McComas, D. J., Phillips, J. L., and Goldstein, B. E.: 1996, in D. Winterhalter, J. T. Gosling, S. R. Habbal, W. S. Kurth, and M. Neugebauer (eds.), 'He Abundance Variations in the Solar Wind: Observations from *Ulysses*', *Solar Wind Eight*, AIP Proc. 382, New York, p. 277.

Borrini, G., Gosling, J. T., Bame, S. J., Feldman, W. C., and Wilcox, J. M.: 1981, 'Solar Wind Helium and Hydrogen Structure Near the Heliospheric Current Sheet: a Signal of Coronal Streamers at 1 AU', *J. Geophys. Res.* **86**, 4565.

Borrini, G., Gosling, J. T., Bame, S. J., and Feldman, W. C.: 1982, 'Helium Abundance Enhancements in the Solar Wind', *J. Geophys. Res.* **87**, 7370.

Dere, K. P.: 1994, 'Explosive Events, Magnetic Reconnection, and Coronal Heating', *Adv. Space Res.* **14**, 13.

Feldman, W. C. and Marsch, E.: 1997, in J. R. Jokipii, J. R. Sonett, C. P. Giampapa, and M. S. Mathews (eds.), 'Kinetic Phenomena in the Solar Wind', *Cosmic Winds and the Heliosphere*, University Arizona Press, Tucson, in press.

Feldman, W. C., Asbridge, J. R., Bame, S. J., and Gosling, J. T.: 1977, in O. R. White (ed.), 'Plasma and Magnetic Fields from the Sun', *The Solar Output and its Variation*, Colorado Associated University Press, Boulder, pp. 351.

Feldman, W. C., Asbridge, J. R., Bame, S. J., Fenimore, E. E., and Gosling, J. T.: 1981, 'The Solar Origins of Solar Wind Interstream Flows Near Equatorial Coronal Streamers', *J. Geophys. Res.* **86**, 5408.

Feldman, W. C., Phillips, J. L., Gosling, J. T., and Isenberg, P. A.: 1996, in D. Winterhalter, J. T. Gosling, S. R. Habbal, W. S. Kurth, and M. Neugebauer (eds.), 'Electron Impact Ionization Rates for Interstellar H and He Atoms Near Interplanetary Shocks: *Ulysses* Observations', *Solar Wind Eight*, AIP Proc. 382, New York, p. 622.

Feldman, W. C., Phillips, J. L., Barraclough, B. L., and Hammond, C. M.: 1996, in K. C. Tsinganos (ed.), '*Ulysses* Observations of the Solar Wind Out of the Ecliptic Plane', *Solar and Astrophysical Magnetohydrodynamic Flows*, Kluwer Academic Publishers, Dordrecht, Holland, pp. 265.

Gosling, J. T.: 1996, in D. Winterhalter, J. T. Gosling, S. R. Habbal, W. S. Kurth, and M. Neugebauer (eds.), 'Magnetic Topologies of Coronal Mass Ejection Events: Effects of 3-Dimensional Reconnection', *Solar Wind Eight*, AIP Proc. 382, New York, pp. 438.

Gosling, J. T. and McComas, D. J.: 1987, 'Field Line Draping About Fast Coronal Mass Ejecta: a Source of Strong out-of-the Ecliptic Interplanetary Magnetic Fields', *Geophys. Res. Letters* **14**, 355.

Gosling, J. T., Pizzo, V., and Bame, S. J.: 1973, 'Anomalously Low Proton Temperatures in the Solar Wind Following Interplanetary Shock Waves: Evidence for Magnetic Bottles', *J. Geophys. Res.* **78**, 2001.

Gosling, J. T., Hildner, E., Asbridge, J. R., Bame, S. J., and Feldman, W. C.: 1977, 'Noncompressive Density Enhancements in the Solar Wind', *J. Geophys. Res.* **82**, 5005.

Gosling, J. T., Asbridge, J. R., Bame, S. J., and Feldman, W. C.: 1978, 'Effects of a Long Entrance Aperture upon the Azimuthal Response of Spherical Section Electrostatic Analyzers', *Rev. Sci. Inst.* **49**, 1260.

Gosling, J. T., Baker, D. N., Bame, S. J., Feldman, W. C., and Zwickl, R. D.: 1987, 'Bidirectional Solar Wind Electron Heat Flux Events', *J. Geophys. Res.* **92**, 8519.

Gosling, J. T.: 1990, in C. T. Russell, E. R. Priest, and L.C. Lee (eds.), 'Coronal Mass Ejections and Magnetic Flux Ropes in Interplanetary Space', *Physics of Magnetic Flux Ropes*, Geophys. Monogr. 58, American Geophys. Union, pp. 343.

Gosling, J.T., Bame, S. J., Feldman, W. C., McComas, D. J., Phillips, J. L., and Goldstein, B. E.: 1993, 'Counterstreaming Suprathermal Electron Events Upstream of Corotating Shocks in the Solar Wind Beyond 2 AU: *Ulysses*', *Geophys. Res. Letters* **20**, 2335.

Gosling, J. T., McComas, D. J., Phillips, J. L., Pizzo, V., Goldstein, B. E., Forsyth, R. J., and Lepping, R. P.: 1995, 'A CME-Driven Solar Wind Disturbance Observed at Both Low and High Heliographic Latitudes', *Geophys. Res. Letters* **22**, 1753.

Hammond, C. M., Feldman, W. C., Phillips, J. L., Goldstein, B. E., and Balogh, A.: 1995, 'Solar Wind Double Ion Beams and the Heliospheric Current Sheet', *J. Geophys. Res.* **100**, 7881.

Hirshberg, J., Bame, S. J., and Robbins, D. E.: 1972, 'Solar Flares and Solar Wind Helium Enrichments: July 1965–July 1967', *Solar Phys.* **23**, 467.

Hundhausen, A. J.: 1977, in J. B. Zirker (ed.), 'An Interplanetary View of Coronal Holes', *Coronal Holes and High Speed Wind Streams*, Colorado Associated University Press, Boulder, p. 225.

Hundhausen, A. J.: 1988, in V. Pizzo, T. E. Holzer, and D.G. Sime (eds.), 'The Origin and Propagation of Coronal Mass Ejections', *Proceedings of the Sixth International Solar Wind Conference*, TN 306+Proc., NCAR, Boulder, pp. 181.

Isenberg, P. A. and Feldman, W. C.: 1995, 'Electron-Impact Ionization of Interstellar Hydrogen and Helium at Interplanetary Shocks', *Geophys. Res. Letters* **22**, 873.

Kennel, C. F., Scarf, F. L., Coroniti, F. V., Russell, C. T., Wenzel, K. P., Sanderson, T. R., Van Ness, P., Feldman, W. C., Anderson, R. R., Scudder, J. D., and Scholer, M.: 1984, 'Plasma and Energetic Particle Structure Upstream of a Quasi-Parallel Interplanetary Shock', *J. Geophys. Res.* **89**, 5419.

Klein, L. W. and Burlage, L. F.: 1982, 'Magnetic Clouds at 1 AU', *J. Geophys. Res.* **87**, 613.

Low, B. C.: 1996, in K. C. Tsinganos (ed.), 'Magnetohydrodynamic Processes in the Solar Corona: Flares, Coronal Mass Ejections and Magnetic Helicity', *Solar and Astrophysical Magnetohydrodynamic Flows*, Kluwer Academic Publishers, Dordrecht, Holland, pp. 133.

Marsden, R. G., Sanderson, T. R., Tranquille, C., Wenzel, K.-P., and Smith, E. J.: 1987, 'ISEE 3 Observations of Low-Energy Proton Bidirectional Events and Their Relation to Isolated Magnetic Structures', *J. Geophys. Res.* **92**, 11009.

McComas, D. J. and Bame, S. J.: 1984, 'Channel Multiplier Compatible Materials and Lifetime Tests', *Rev. Sci. Inst.* **55**, 463.

McComas, D. J., Gosling, J. T., Phillips, J. L., Bame, S. J., Luhmann, J. G., and Smith, E. J.: 1989, 'Electron Heat Flux Dropouts in the Solar Wind: Evidence for Interplanetary Magnetic Field Reconnection?', *J. Geophys. Res.* **94**, 6907.

McComas, D. J., Gosling, J. T., Hammond, C. M., Moldwin, M. B., and Phillips, J. L.: 1994, 'Magnetic Reconnection Ahead of a Coronal Mass Ejection', *Geophys. Res. Letters* **21**, 1751.

McComas, D. J., Balogh, A., Bame, S. J., Barraclough, B. L., Feldman, W. C., Forsyth, R., Funsten, H. O., Goldstein, B. E., Gosling, J. T., Neugebauer, M., Riley, P., and Skoug, R.: 1998, '*Ulysses*' Return to the Slow Solar Wind', *Geophys. Res. Letters* **25**, 1.

Montgomery, M. D., Asbridge, J. R., Bame, S. J., and Feldman, W. C.: 1974, 'Solar Wind Electron Temperature Depressions Following Some Interplanetary Shock Waves: Evidence for Magnetic Merging', *J. Geophys. Res.* **79**, 3103.

Parker, E. N.: 1958, 'Dynamics of the Interplanetary Gas and Magnetic Fields', *Astrophys. J.* **128**, 664.

Petschek, H. E.: 1964, 'Magnetic Field Annihilation, AAS-NASA Symposium on the Physics of Solar Flares', *NASA Spec. Publ.*, SP-50, pp. 425.

Phillips, J. L., Gosling, J. T., McComas, D. J., Bame, S. J., and Feldman, W. C.: 1992, in S. Fischer and M. Vandes (eds.), 'Magnetic Topology of Coronal Mass Ejections Based on ISEE-3 Observations of Bidirectional Electron Fluxes at 1 AU', in *Proc. First SOLTIP Symp.*, Vol. 2, Astron. Inst. Czech Academy of Science Press, Prague, pp. 165.

Phillips, J. L., Bame, S. J., Barnes, A., Barraclough, B. L., Feldman, W. C., Goldstein, B. E., Gosling, J. T., Hoogeveen, G. W., McComas, D. J., Neugebauer, M., and Suess, S. T.: 1995, *Geophys. Res. Letters* **22**, 3301.

Sheeley, N. R., Bohlin, J. D., Brueckner, G. E., Purcell, J. D., Scherrer, V. E., and Tousey, R.: 1975, 'The Reconnection of Magnetic Field Lines in the Solar Corona', *Astrophys. J.* **196**, 129.

Tsuneta, S.: 1996, in K. C. Tsinganos (ed.), 'The Dynamic Solar Corona in X-rays with *Yohkoh*', *Solar and Astrophysical Magnetohydrodynamic Flows*, Kluwer Academic Publishers, Dordrecht, Holland, pp. 85.

Von Steiger, R. and Geiss, J.: 1989, 'Supply of Fractionated Gases to the Corona', *Astron. Astrophys.* **225**, 222.

Zwickl, R., Doggett, K., Sahm, S., Barrett, W., Grubb, R., Detman, T., Raben, V., Smith, C., Riley, P., Gold, R., Mewaldt, R., and Maruyama, T.: 1998, 'The NOAA Real-Time Solar-Wind (RTSW) System Using ACE Data', *Space Sci. Rev.* **86**, 633.